Quantifying the internal and external drivers of Southeast Asian rainfall extremes on decadal timescales

Climate Dynamics
https://doi.org/10.1007/s00382-024-07412-x

ORIGINAL ARTICLE

Quantifying the internal and external drivers of Southeast Asian rainfall extremes on decadal timescales

Shouyi Wang[1,2] · Caroline C. Ummenhofer[2] · Sujata A. Murty[3] · Hung T. T. Nguyen[4,5] · Brendan M. Buckley[5]

Received: 7 February 2024 / Accepted: 18 August 2024

Abstract

Rainfall over mainland Southeast Asia experiences variability on seasonal to decadal timescales in response to a multitude of climate phenomena. Historical records and paleoclimate archives that span the last millennium reveal extreme multi-year rainfall variations that significantly affected the societies of mainland Southeast Asia. Here we utilize the Community Earth System Model Last Millennium Ensemble (CESM-LME) to quantify the contributions of internal and external drivers to decadal-scale rainfall extremes in the Southeast Asia region. We find that internal variability was dominant in driving both Southeast Asian drought and pluvial extremes on decadal timescales although external forcing impacts are also detectable. Specifically, rainfall extremes are more sensitive to Pacific Ocean internal variability than the state of the Indian Ocean. This discrepancy is greater for droughts than pluvials which we suggest is attributable to external forcing impacts that counteract the forced Indian Ocean teleconnections to Southeast Asia. Volcanic aerosols, the most effective radiative forcing during the last millennium, contributed to both the Ming Dynasty Drought (1637–1643) and the Strange Parallels Drought (1756–1768). From the Medieval Climate Anomaly to the Little Ice Age, we observe a shift in Indo-Pacific teleconnection strength to Southeast Asia consistent with enhanced volcanism during the latter interval. This work not only highlights asymmetries in the drivers of rainfall extremes but also presents a framework for quantifying multivariate drivers of decadal-scale variability and hydroclimatic extremes.

Keywords Southeast Asia · Rainfall extremes · Last millennium · Internal variability · External forcing

1 Introduction

As a consequence of the large-scale Asian monsoon circulation, mainland Southeast Asia (MSEA) receives the majority of its annual rainfall during the boreal summer months (June–September, JJAS). Data from the instrumental era (1900 CE–present) reveal that this monsoonal rainfall exhibits interannual and decadal variability in spatial extent, magnitude, and timing (Phan-Van et al. 2022; Skliris et al. 2022). Prior to the 20th century, paleoclimate archives and historical records reveal that throughout the last millennium (850 CE–to present) multi-year intervals of severe collapse or intensification of the MSEA monsoon dramatically affected regional societies (Buckley et al. 2007, 2014; Cook et al. 2010, 2022; Wang et al. 2019). Indeed, periods of societal change and civil unrest throughout Asia have been partially attributed to these extreme hydroclimate excursions. The collapse of Angkor Wat as the capital city of the Khmer empire has been determined to be partially a result of the Angkor droughts interspersed by severe flooding in the late

✉ Shouyi Wang
syiwang@mit.edu

Caroline C. Ummenhofer
cummenhofer@whoi.edu

Sujata A. Murty
smurty@albany.edu

Hung T. T. Nguyen
hungn@illinois.edu

Brendan M. Buckley
bmb@ldeo.columbia.edu

[1] MIT-WHOI Joint Program in Oceanography, Cambridge, MA, USA

[2] Woods Hole Oceanographic Institution, Woods Hole, MA, USA

[3] University at Albany, State University of New York, Albany, NY, USA

[4] University of Illinois Urbana-Champaign, Urbana, IL, USA

[5] Lamont-Doherty Earth Observatory, Palisades, NY, USA

Published online: 12 September 2024

14th to 15th century (Buckley et al. 2010; Penny et al. 2018). In addition, an extended drought from 1637–1643 played a significant role in the subsequent collapse of the Ming Dynasty in 1644 (Chen et al. 2020; Cook et al. 2010; Zheng et al. 2014). While rainfall extremes of comparable magnitude and duration have not been observed in the instrumental era, global climate models predict that the intensity and duration of both wet and dry extremes in the MSEA region should increase under global warming (Stevenson et al. 2022; Supharatid and Nafung 2021). Understanding the drivers of historical low-frequency hydroclimate excursions will be important for assessing future hydrological changes in the MSEA region. We provide a brief overview of various drivers of Asian monsoon variability across a range of timescales to contextualize the current study of decadal-scale precipitation extremes, with a particular focus on drivers arising from internal climate variability versus those due to external forcing.

The seasonal rainfall cycle over MSEA displays variability across a range of timescales in response to oscillations internal to the climate system. On intra-seasonal timescales (20–90 days), the Madden–Julian Oscillation has been shown to modulate the frequency of Southeast Asia extreme rain events during boreal winter through its effects on local convective activity (Xavier et al. 2014). On interannual timescales (3–8 years), numerous studies have found that MSEA rainfall is influenced by phasing of the adjacent Pacific and Indian Oceans, namely the El Niño-Southern Oscillation (ENSO; Cherchi and Navarra 2013; Hau et al. 2023; Hernandez et al. 2015; Hu et al. 2022, 2023; Li et al. 2024; Ummenhofer et al. 2013; Wang et al. 2024; Webster et al. 1998; Yu et al. 2018) as well as the Indian Ocean Dipole (IOD; Ashok et al. 2001; Ge et al. 2021; Saji et al. 1999; Yuan et al. 2008). Both ENSO and IOD can influence the strength of the Walker circulations over the Indo-Pacific, leading to changes in the magnitude of moisture convergence and ascent over the Indo-Pacific Warm Pool (IPWP). On decadal-multidecadal timescales (10–100 years) modes of variability in the Pacific and Atlantic Ocean, namely the Interdecadal Pacific Oscillation (IPO) and Atlantic Multidecadal Oscillation (AMO), have been found to influence Asian monsoon rainfall (Hrudya et al. 2021; Krishnamurthy and Krishnamurthy 2014; Yang et al. 2017; Yu et al. 2018). Not only can these internal modes independently affect MSEA hydroclimate, but their interactions with each other must also be considered. Coinciding El Niño and +IOD events have been shown to result in more severe drought across Southeast Asia (Cherchi and Navarra 2013; Ummenhofer et al. 2013; Xiao et al. 2022). In addition, climate modes across different timescales can interact with each other resulting in a diverse range of teleconnection patterns. For example, the relationship between ENSO and the Asian monsoon has been shown to exhibit decadal variability as a consequence of IPO and AMO phasing (Buckley et al. 2019; Chan and Zhou 2005; Hau et al. 2023; Krishnamurthy and Krishnamurthy 2014; Krishnan and Sugi 2003; Lu et al. 2006; Wang et al. 2024; Xu et al. 2021).

The last millennium is also characterized by variability in external forcings which have also been linked to monsoonal rainfall over Asia (Mohtadi et al. 2016; Sinha et al. 2011, 2015). Prior to the instrumental era, these external drivers were mostly solar irradiance and aerosols from volcanic eruptions (Chen et al. 2020; Du et al. 2023; Narasimha et al. 2010; Jin et al. 2019; Stevenson et al. 2016; Tejedor et al. 2021). External forcings can both directly contribute to hydrological cycle changes both by modifying the radiative fluxes in the atmosphere and indirectly through interactions with internal climate modes. Indeed, previous studies have highlighted that, akin to low-frequency internal modes, solar irradiance variability can modulate ENSO's spatial footprint over monsoon Asia (Du et al. 2023; Jin et al. 2019; Narasimha et al. 2010) on (multi)decadal timescales. Modeling studies have found that volcanic eruptions of sufficient magnitude trigger an El Niño/+IPO like response in the Pacific and a -IOD like response in the Indian Ocean (Izumo et al. 2018; Khodri et al. 2017; Maher et al. 2015; Stevenson et al. 2016; Sun et al. 2022; Tiger and Ummenhofer 2023). It is worth noting that several proxy-based studies have identified discrepancies between numerical models and climate archives in the tropical hydroclimate and ENSO response to volcanism (Anchukaitis et al. 2010; Dee et al. 2020; Tejedor et al. 2021; Zhu et al. 2022), highlighting potential biases in the simulated response to volcanic forcing. These discrepancies are considered for the current model-based study and are discussed in the conclusion.

While the links between decadal climate modes, external forcings, and the Asian monsoon have been previously investigated, prior studies have largely focused on the spatial patterns of teleconnections and/or the low-frequency modulation of the ENSO-Asian monsoon relationship (Chan and Zhou 2005; Hrudya et al. 2021; Krishnamurthy and Krishnamurthy 2014; Krishnan and Sugi 2003; Wang et al. 2024; Yang et al. 2017; Yu et al. 2018). Here we focus on quantifying the drivers of rainfall excursions for MSEA on a specific timescale (10–50 years) and aim to address several key questions. Do last millennium external forcings meaningfully contribute to decadal-scale extremes either directly or indirectly? How does the frequency and magnitude of rainfall extremes depend on the Pacific Ocean and Indian Ocean states? How do these relationships between Indo-Pacific modes, external forcings, and MSEA rainfall vary for positive rainfall (pluvial) and negative rainfall (drought) anomalies?

To address these questions we utilize the Community Earth System Model Last Millennium Ensemble (CESM-LME; Otto-Bliesner et al. 2016). The CESM-LME consists

of multiple realizations of global climate under identical external forcings which allows for the separation of internal and external drivers akin to previous ensemble simulation studies (Deser et al. 2012, 2020; Maher et al. 2020). Additionally, each LME simulation spans over 1000 model years (850–2005 CE), this providing a sufficiently large sample size for robust probabilistic analysis of extremes on decadal timescales. The remainder of the paper is structured as follows: Sect. 2 introduces the observational datasets, climate model, rainfall extremes classification, and significance testing. In Sect. 3 we provide model validation by assessing model-simulated MSEA rainfall variability and relationship to climate modes. The relative contributions of internal variability and external forcings are quantified in Sect. 4. Section 5 characterizes the sensitivity of MSEA rainfall extremes to Pacific and Indian Ocean internal modes. In Sect. 6 the impacts of last millennium external forcings throughout the last millennium is assessed. Section 7 summarizes the findings of this study.

2 Data and methods

2.1 Observational data

Monthly output from the Global Precipitation Climatology Centre Full Data Product (GPCC) is used to assess and validate the climate model's characterization of MSEA rainfall (Schneider et al. 2016). GPCC is a global rainfall product based on global quality controlled rainfall station data that spans 1891–2019. In this study we utilize the gridded GPCC V2020 product at $0.5° \times 0.5°$ resolution. Sea surface temperature (SST) data is also used to assess the model representation of the relationship between various climate modes (characterized by SST patterns) and MSEA rainfall. Here we use the Extended Reconstructed Sea Surface Temperature version 5 (ERSSTv5) which provides global monthly values for 1854–2023. ERSSTv5 is derived from statistical interpolation of SST measurements from the International Comprehensive-Atmosphere Dataset version 3 (Huang et al. 2017). Model validation of the relationship between SST patterns and MSEA rainfall is also conducted using the Hadley Centre Global Sea Ice and Sea Surface Temperature (HadISST, Rayner et al. 2003) and results were largely consistent with ERSST analysis (Supplementary Fig. 1 g–i).

Climate indices used in this study for model validation and analysis are constructed using SST regions as follows: IOD is defined as the anomalous SST gradient between the western equatorial Indian Ocean (50°E – 70°E and 10°S – 10°N) and the southeastern equatorial Indian Ocean (90°E – 110°E and 10°S – 0°N) (Saji et al. 1999); ENSO is defined as SST anomalies in the Nino3.4 region (170°E – 120°W and 5°S – 5°N) (Trenberth 1997); IPO is defined as the difference between the eastern equatorial Pacific (170°E – 90°W and 10°S – 10°N) and the average anomalies in the northwestern Pacific (140°E – 145°W and 25°N – 45°N) and southwestern Pacific (150°E – 160°W and 50°S – 15°S) (Henley et al. 2015).

2.2 Climate model

The CESM-LME utilizes the CESM1.1 configuration at 2° resolution in the atmosphere and land models and 0.3° to 1° in the ocean model. The LME consists of 36 simulations of global climate from 850–2005 CE using reconstructions (Gao et al. 2008; Vieira et al. 2011) and theory to inform the transient evolution of model external forcings including solar irradiance, volcanic emissions, greenhouse gases, land-use/land-cover, and orbital parameters. Of the 36 simulations, 13 ensemble members are forced with all transient forcings (all-forcing ensemble). Smaller ensembles are simulated with only one external forcing type varying transiently. Each LME simulation is initialized with an extremely small random roundoff difference (order 10^{-14} °C) in the global temperature field which quickly grows within the coupled system to produce internal variability unique to each ensemble member. The CESM-LME is the largest of these ensemble simulations for the last millennium, making it an ideal venue for exploring last millennium internal vs external drivers. Indeed, the LME has been used extensively to study last millennium Indo-Pacific climate drivers (Abram et al. 2020; Atwood et al. 2021; Liu et al. 2022; Roldán–Gmez et al. 2022; Stevenson et al. 2016, 2019; Tiger and Ummenhofer 2023) and Asian Summer Monsoon variability (Denniston et al. 2016; Fu et al. 2024; Shi et al. 2018; Wang et al. 2019, 2024). We further assess the LME skill in characterizing MSEA rainfall variability on various timescales relevant for the current study in Sect. 3.

2.3 Rainfall extremes classification

In this study we define MSEA rainfall as the average rainfall in the Fig. 1a box (95°E – 110°E;10°N – 22°N) and classify extremes using the peaks-over-threshold framework common to extreme value theory (Naveau et al. 2005). Though the term "extreme" traditionally refers to high-frequency synoptic to interannual excursions rather than decadal-scale anomalies, we find the term appropriate here given that we apply many of the analytical methods from high-frequency hydroclimate extremes to these longer timescales (Hariadi et al. 2024; Kim et al. 2019; Naveendrakumar et al. 2019). We set the condition for extreme events as years when the annual MSEA rainfall anomaly is outside of the middle 95% of the distribution (5% threshold). Thus years of MSEA rainfall higher than 97.5% are classified as "pluvial extremes"

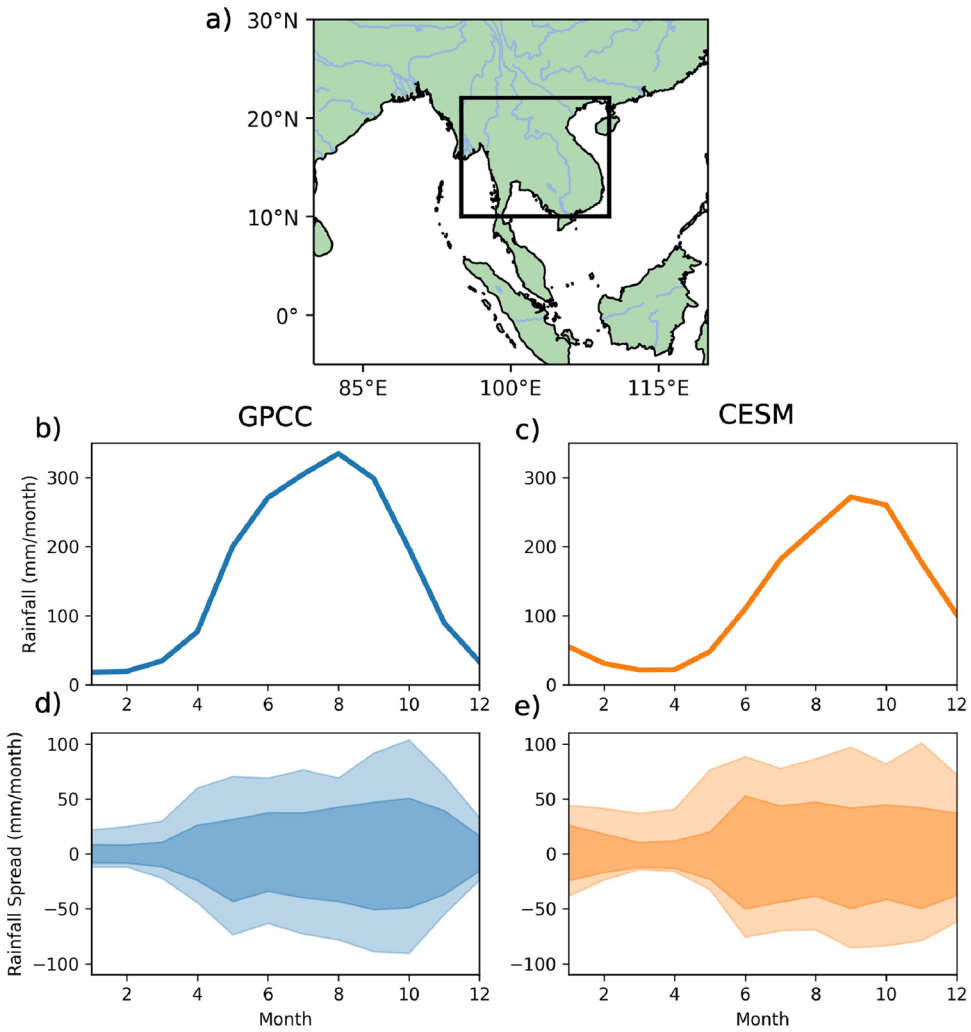

Fig. 1 Geographical region of mainland Southeast Asia with a box indicating the domain (95°E – 110°E;10°N – 22°N) that defines MSEA rainfall for this study **(a)**. Long-term average monthly climatology of MSEA rainfall in GPCC **(b)** and CESM **(c)**. Amplitude of variability (spread) for each month within the 68% (1σ, dark shading) and 95% (2σ, light shading) of MSEA rainfall in GPCC **(d)** and CESM **(e)**. All long-term averages and ranges are calculated over the 1901–2005 period. Data from all 13 CESM all-forcing ensemble members are utilized here

and years less than 2.5% are defined as "drought extremes." Because the 13 all-forcing ensemble members have identical model configurations and transient forcings, the percentile-based thresholds for drought and pluvials were determined from the entire distribution of all-forcing ensemble simulations. Much of the analysis in this study was repeated using two additional MSEA rainfall thresholds (2% and 10% thresholds) to ensure that the findings were robust.

We utilize annually averaged (Jan–Dec) rainfall anomalies for extremes classification rather than sub-sampling for the summer monsoon season. While the majority of rainfall occurs during the summer monsoon, rainfall anomalies of equal magnitude could be found in the adjacent shoulder months (Fig. 1d, e), justifying this approach. Dry summer monsoon months could be compensated by anomalously wet transition months and vice versa. Furthermore, the timings of monsoon season onset and withdrawal change from year to year (Cook et al. 2009; Nguyen et al. 2022). Annual mean rainfall anomalies better reflect total time-integrated water resource changes on decadal timescales and should therefore be more relevant for assessing potential impacts on society (Milly 1994). Focusing on decadal timescales, all model variables (rainfall, moisture, SST, winds) analyzed in this study are first filtered using a Butterworth band-pass filter (window = 10–50 years, order = 5). Consistent with the validation analysis (Fig. 2), all SST modes are calculated for the preceding hydrological year (prior June–May) of the rainfall extreme.

2.4 Significance testing

Because we filter the LME output to isolate decadal-scale variablity, our data has high autocorrelation and a reduced number of effective degrees of freedom. Traditional significance tests which assume independent sampling are therefore inappropriate here. To mitigate this issue, we employ Monte-Carlo resampling along with timeseries phase scrambling (Ebisuzaki 1997) to properly estimate the significance of our results. Monte-Carlo resampling involves either repeatedly shuffling the original dataset or randomly sampling the dataset to

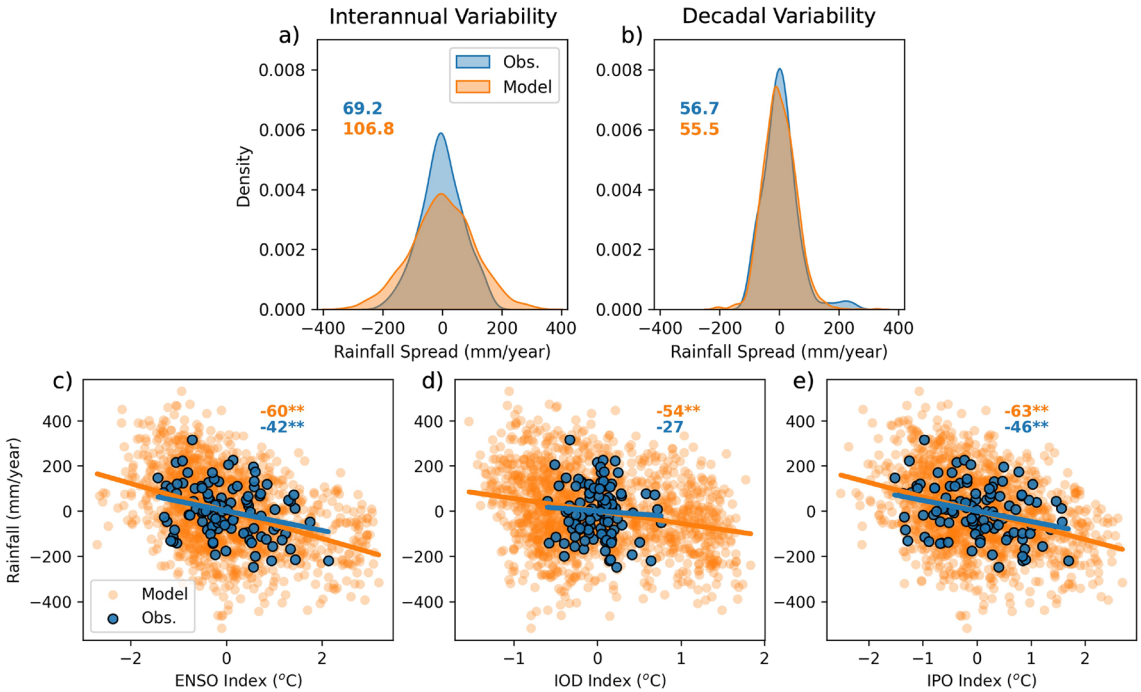

Fig. 2 Probability density function (PDF) of rainfall anomalies on interannual **(a)** and decadal **(b)** timescales in observations (blue) and model (orange) isolated using bandpass filtering (3–8 years for interannual and 10–50 years for decadal). The relationship between unfiltered indices indicative of ENSO **(c)**, IOD **(d)**, and IPO **(e)** and MSEA rainfall are shown for observations (blue) and CESM model (orange) for individual years (scatterpoints) and linear regression (line) and regression slope values (numbers). MSEA rainfall anomalies are averaged over the calendar year (January–December) while climate mode anomalies are averaged over the preceding hydrological year (prior June–May as justified in the text). All values are from 1901–2005 in both observations and model. Data from all 13 CESM all-forcing ensemble members are utilized here. Slope values significant at the 5% level determined from phase-scrambling Monte-Carlo simulations are indicated by **

construct a large number of synthetic samples that could be used to construct a null-hypothesis distribution for significance testing. Conventional shuffling and random sampling break down the autocorrelation of filtered data, thus we utilize phase scrambling to shuffle the LME dataset while preserving its autocorrelation. Phase scrambling is a technique in which a time series is decomposed into its principle fourier modes and its phases are randomly shifted before reconstructing the time-series back together (Ebisuzaki 1997). This produces a "scrambled" version of the timeseries that shares an identical power spectrum and distribution of values but is entirely uncorrelated with the original data in time. By phase-scrambling and recomputing the metric of interest 1000 times, we produce a null distribution that preserves the auto-correlation of the underlying dataset. Composite anomalies and regression slope values in this study are deemed significant (at the 5% level) if they are outside the 2.5% and 97.5% of this distribution.

3 Model validation

Before analyzing the filtered LME model output for drivers of decadal rainfall extremes, we assess its skill in reproducing observed seasonal to decadal variability by comparing the observational datasets to CESM over the common overlapping period 1901–2005 (Figs. 1, 2). CESM reasonably captures the overall structure of the MSEA seasonal cycle. However, the timing of summer monsoon rainfall slightly deviates from observations, with the model producing a weaker and slightly delayed peak summer monsoon (Fig. 1b, c). On the other hand, the amplitude of rainfall variance (spread) is simulated reasonably well, with largely equal magnitude variations from monsoon onset through peak summer monsoon to withdrawal (Fig. 1d, e) and less rainfall variability during

winter monsoon months. Importantly, CESM skillfully reproduces that the monsoon transition months exhibit high amplitude variations despite lower absolute rainfall relative to peak monsoon, likely due to influences of Indo-Pacific SST anomalies on the monsoon transitions (Cook et al. 2009; Ge et al. 2021; Nguyen et al. 2022).

To assess the model's characterization of interannual and decadal variability, we compare the distributions of rainfall anomalies between GPCC and CESM after band-pass filtering (using a butterworth order = 5 filter) to isolate these frequencies (3–8 years for interannual; 10–50 years for decadal). On interannual timescales, the model overestimates the variance of the distribution (69.2 in GPCC vs 106.8 in CESM; Fig. 2a) while on decadal timescales the variance magnitude is more accurately represented (56.7 in GPCC vs 55.5 in CESM; Fig. 2b). The agreement in the amplitude of decadal-scale variability supports utilizing CESM for the present study of decadal-scale climate variability.

The relationship between dominant Indo-Pacific climate modes (ENSO, IOD, and IPO) and MSEA rainfall is also assessed by comparing unfiltered annual climate indices to annual rainfall anomalies over the overlapping 1901–2005 period for observations and CESM (Fig. 2c–e). Climate index values are derived from SST anomalies averaged over the hydrological year (June–May) that precedes each rainfall anomaly calendar year (January–December). This slight offset is chosen because the prior hydrological year captures the development and peak of climate modes (September–November for IOD and December–February for ENSO) which has been shown to strongly influence subsequent-year monsoon rainfall (Ge et al. 2021; Yuan et al. 2008). For both the observational datasets and CESM, there exists a negative relationship between climate indices and MSEA rainfall (Fig. 2c–e), consistent with prior studies (Cherchi and Navarra 2013; Li et al. 2024; Ummenhofer et al. 2013, 2024; Xiao et al. 2022). The choice for the staggered SST indices is further supported by consistent negative correlation between SST modes during prior boreal winter months (SON, DJF) and subsequent annual MSEA rainfall (Supplementary Fig. 1d–f). It is worth noting that linear regression reveals that these negative correlations are systematically stronger in CESM than the observations (Fig. 2c–e). Additionally, while all teleconnections in CESM are significant at the 5% level, the observed relationship between IOD and MSEA rainfall is not significant at the 5% level (Fig. 2d). This could be partially a consequence of the sparsity of in-situ SST data in the Indian Ocean during the first half of the 20th century. Reproducing these relationships for 1960–2005 reveals a significant link between IOD and MSEA rainfall (Supplementary Fig. 1b) however this slope in observations is steeper than in the model. These data-model discrepancies in slope values could be attributed to CESM model biases in the eastern Pacific cold-tongue or IPWP representation (Flato et al. 2014; Guilyardi et al. 2009; Jiang et al. 2021; Taschetto et al. 2014; Wieners et al. 2019; Wu et al. 2022). While important to consider, these offsets in teleconnection strength do not preclude the current study which aims to understand the various contributions to MSEA rainfall extremes within a single dynamically-consistent modeling framework. Caveats in the interpretation of model results are discussed in the conclusion.

Overall, CESM skillfully reproduces key aspects of the MSEA monsoon, such as the modulation of monsoon onset and withdrawal (Fig. 1d, e), the amplitude of decadal-scale rainfall variability (Fig. 2b), as well as the relationships between MSEA rainfall and Indo-Pacific climate modes (Fig. 2c–e). We therefore determine that the CESM-LME is appropriate for studying the drivers of decadal rainfall extremes in the context of this study.

4 Assessing internal and external relative contributions

Applying the 5% extreme threshold on the 13 all-forcing ensemble members of the LME, we identified 125 drought extremes and 141 pluvial extremes ranging from 1–6 years in duration among all 13 ensemble members. We isolated the internal and external contributions to these rainfall extremes by subtracting the ensemble mean anomaly from each drought and pluvial following:

$$R_{IC} = R - R_{EM} \tag{1}$$

where R is the total rainfall extreme anomaly of each extreme event with respect to its own timeseries (in mm/year), R_{EM} is the ensemble mean rainfall anomaly across the 13 all-forcing LME members at the same time step, and R_{IC} is the difference between the two, reflective of the internal climate contribution to the rainfall extreme. Figure 3 visualizes the decomposition of these extremes into their internal and external components. We see that the internal contribution for most pluvial (drought) extremes hover around 100 to 140 mm/year (− 100 to − 140 mm/year; Fig. 3a, b). However, when the ensemble mean is exceptionally large in magnitude (Fig. 3a black line), R_{IC} approaches zero, illustrating intervals when external forcings can dominate the rainfall extreme signal with less contribution from internal modes.

To assess the significance of external forcing contributions, we construct synthetic versions of the 13 all-forcing rainfall timeseries using phase-scrambling (Sect. 2.4) and pass them through the same pipeline as our analysis (identify peaks-over-threshold extremes and estimate R_{IC}). Because these synthetic ensembles share no external forcings with each other, their drought and pluvial R_{IC} values arise entirely from random chance, providing an ideal null-hypothesis to

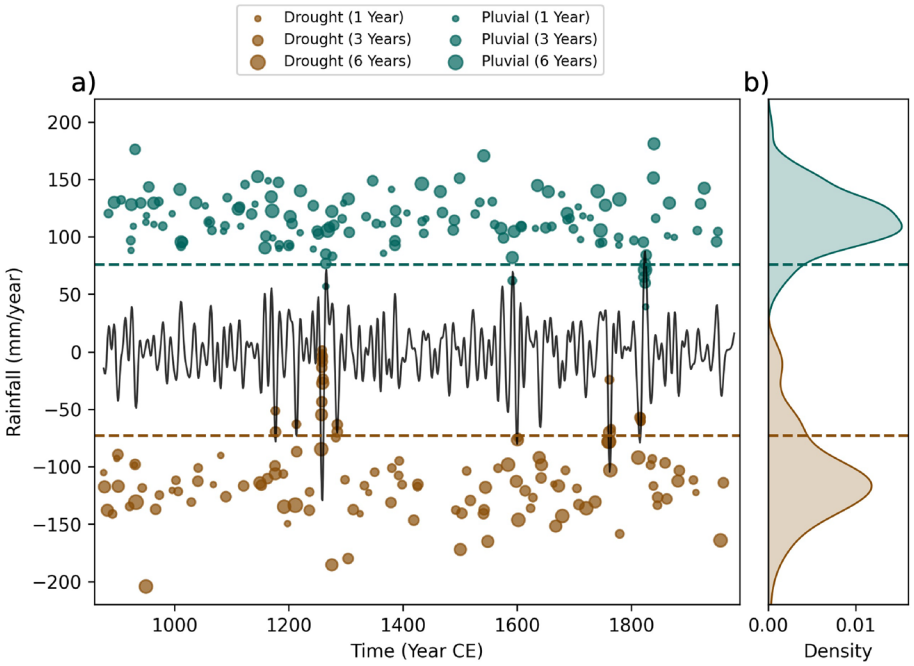

Fig. 3 Drought (brown circles) and pluvial (green circles) extremes magnitude associated with internal variability (R_{IC}) along with the ensemble mean rainfall anomaly (black line) over the last millennium **(a)**. The size of the circles scales to the length of the rainfall extreme, ranging from 1–6 years. The PDF distribution of R_{IC} values for all drought and pluvial extremes **(b)**. Brown (green) dashed lines correspond to the 5% significance threshold of R_{IC} for drought (pluvial) extremes determined from phase scrambling

assess the significance of last millennium external forcings. This phase scrambling is conducted 1000 times to produce a large distribution of null-hypothesis drought (pluvial) R_{IC} values and the 95% (5%) of this distribution is used as the significance threshold (Fig. 3 dashed lines) for LME drought (pluvial) extremes. Consequently, drought and pluvial extremes that lie between these two dashed lines contain significant external contributions.

The R_{IC} of LME drought extremes largely lie below the significance threshold (Fig. 3a brown dashed line) except for a cluster of droughts in the late 1100–1200s and late 1700–1800s where R_{IC} of droughts are near zero (Fig. 3a brown circles) and the ensemble mean (Fig. 3a black line) exhibits large negative excursions. For pluvial extremes, the mid 1200s and early 1600s stand out as two periods where external forcings potentially play a role in contributing to significantly reduced R_{IC} anomalies (Fig. 3a green circles). Examining the total distributions we see that while a majority of droughts and pluvials fall outside of the significance thresholds (Fig. 3b PDFs vs dashed lines), the drought distribution has a longer tail towards zero (more external forcing contributions) than the pluvials. Specifically, 15% of droughts have significant external contributions (Fig. 3b brown PDF vs dashed line) whereas only 5% of pluvials are significantly impacted by external forcings (Fig. 3b green PDF vs dashed lines). These findings suggest that decadal-scale drought and pluvial extremes are both largely driven by internal variability. However, external forcings do impact several rainfall extremes, with more of an influence towards drought extremes than pluvial extremes (Fig. 3b brown vs green PDFs). These externally forced rainfall extremes are explored further in Sect. 6. Identical analysis using two different extremes thresholds (2% and 10%) produced qualitatively similar results (Supplementary Figs. 2, 3). Analysis using two different filtering windows (10–40 years and 10–60 years) also yielded similar results (Supplementary Fig. 4).

Our analysis of relative contributions suggests that MSEA rainfall extremes are largely associated with internal variability of the climate system. We provide spatial context for this through composite analysis of rainfall, moisture divergence, atmospheric circulation, and SST during all drought and pluvial extremes (Fig. 4). We see that these decadal-scale excursions are associated with broad-scale rainfall and low-level (850 hPa) winds anomalies throughout the tropical Indo-Pacific characterized by a zonal precipitation tripole centered on the IPWP (Fig. 4a, b). These rainfall tripole patterns can be understood as a consequence of changes in lower tropospheric (1000–700 hPa) moisture transport (Fig. 4c, d) as well as modulations in low-level atmospheric ascent (Fig. 4e, f) which both exhibit similar spatial patterns during MSEA extremes. While the vertically-integrated moisture divergence analysis here (VIMD; Fig. 4c, d) does not explicitly isolate the thermodynamic, dynamic, and nonlinear contributions to lower tropospheric moisture, previous studies have found that Indo-Pacific tropical modes (ENSO, IPO, and IOD) influences tropical moisture through both dynamical and thermodynamic processes (Taschetto et al. 2020; Ummenhofer et al. 2021; Wang et al. 2003). Indeed the similar spatial patterns between VIMD and lower tropospheric vertical velocity (Fig. 4c, d vs Fig. 4e, f) confirms the dynamical contributions to moisture divergence.

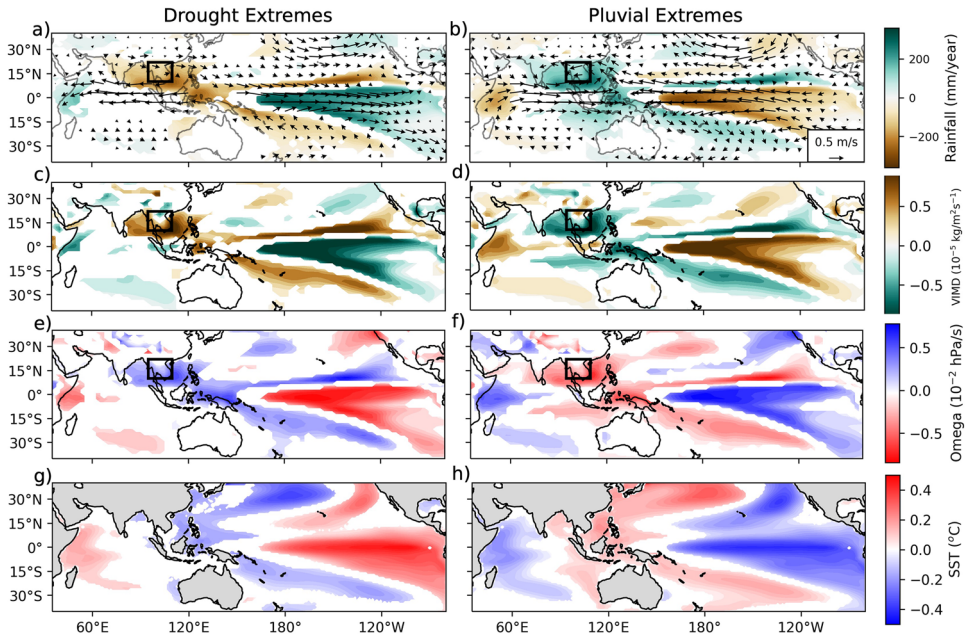

Fig. 4 Composite rainfall (colors) and 850 hPa wind anomalies (vectors) during MSEA drought **(a)** and pluvial **(b)** extremes. Vertically integrated moisture divergence (VIMD) in the lower troposphere (1000–700 hPa) anomalies during drought **(c)** and pluvial **(d)** extremes. Vertical velocity anomalies at 700 hPa during drought **(e)** and pluvial **(f)** intervals where negative (positive) anomalies reflect upward (downward) motion. SST anomalies during drought **(e)** and pluvial **(f)** extremes. SST anomalies are shown for the hydrological year leading up to rainfall extremes (prior June–May) while all other variables are derived for the calendar year of rainfall extremes. All results are shown for the 13 all-forcing LME ensemble members. Black box in **(a–f)** corresponds to MSEA region used to define extremes. Only anomalies significant at the 5% are shown using phase-scrambling Monte-Carlo simulations

On decadal timescales, these atmospheric circulation and moisture changes are tied to the underlying SST through the Bjerknes feedback which are largely ENSO and IPO-like in the Pacific Ocean and IOD-like in the Indian Ocean (Fig. 4g, h).

Overall, MSEA drought extremes are driven by +IPO, El Niño, and +IOD-like SST patterns which weaken the zonal SST gradients. Through air-sea interactions this weakens the Indo-Pacific Walker circulations, reducing moisture transport and generating anomalous descent to the MSEA region which ultimately reduces rainfall (Fig. 4a, c, e, g). Conversely the -IPO, La Niña, and -IOD anomalies during MSEA pluvials strengthen the Walker circulation and increase moisture transport and ascending motion over the warm-pool region which enhances rainfall (Fig. 4b, d, f, h). These composite anomalies are consistent across multiple extremes thresholds (Supplementary Figs. 5, 6). It is worth noting that MSEA rainfall excursions are coherent with the South Asian monsoon (Fig. 4a, b) but do not appear to coincide with significant anomalies in other land monsoon regions such as East Asia or North America (Fig. 4a, b). This highlights that MSEA extremes are dominated by internal variations of regional Indo-Pacific modes and not by global external forcings. To a first order, the zonal tripole anomalies over the Indo-Pacific are symmetric between wet and dry extremes. However there are some noticeable differences, such as the eastern Indian Ocean which does not display significant anomalies during droughts but does so during pluvials. We explore the influence of individual ocean basins and their potential non-linear impacts on MSEA rainfall in the next section.

5 Sensitivity to Indo-Pacific internal modes

Because composite analysis reveals the strong link between decadal-scale extremes and the Indo-Pacific climate variability, we focus on clarifying the relationship between regional Indo-Pacific modes of variability (IPO and IOD) and MSEA rainfall extremes on decadal timescales. The linkage between these tropical modes and MSEA rainfall is further confirmed by power spectral density analysis, which highlights spectral peaks aligned between rainfall and Indo-Pacific SST modes (Supplementary Fig. 7). We acknowledge that while Atlantic Ocean SST can affect monsoon Asia through atmospheric teleconnections (Krishnan and Sugi 2003; Lu et al. 2006), these relationships are indirect and occur on timescales longer than the focus of this study (60–80 years). Additionally, on decadal timescales the Pacific Ocean is

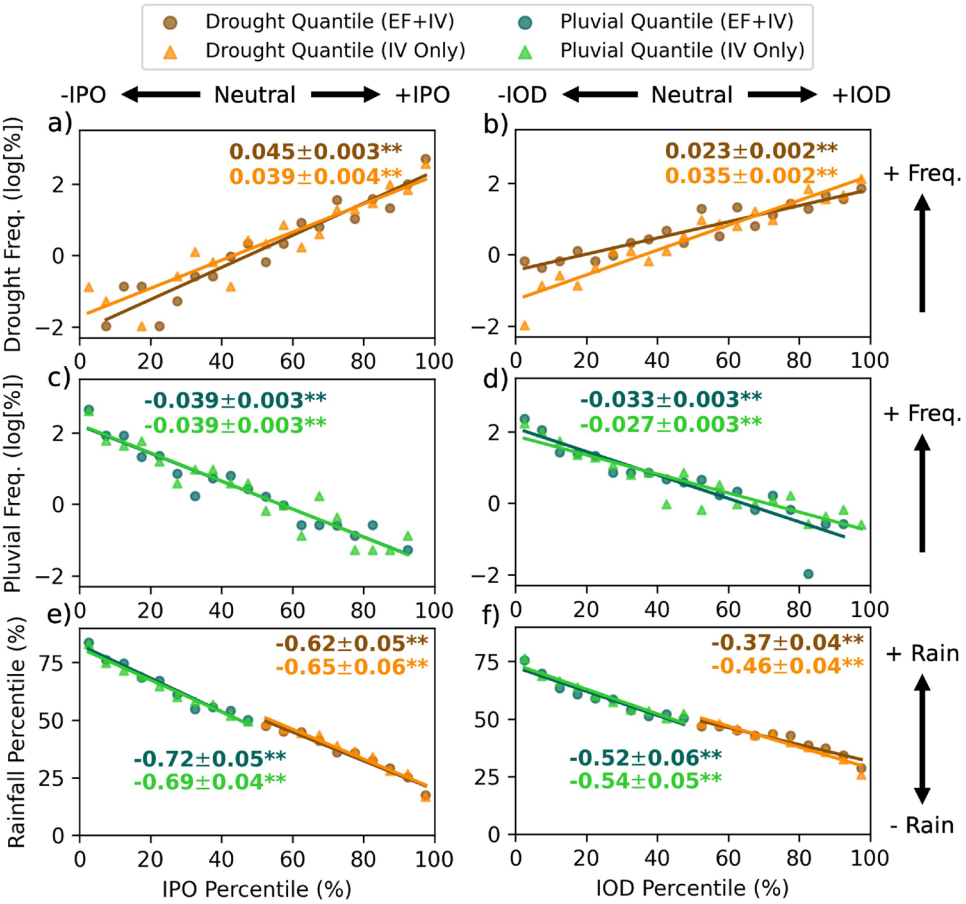

Fig. 5 The frequency of MSEA drought extremes (brown circles) **(a)** and the frequency of pluvial extremes (green circles) **(c)** as a function of IPO state calculated for every 5% quantile. Linear regression (lines) and corresponding slopes with one standard error (numbers) of these relationships are visualized. Complementary sampling of the LME based on IOD state for drought **(b)** and pluvial **(d)** frequencies are shown. The magnitude of MSEA dry and wet anomalies as a function of IPO **(e)** and IOD **(f)** state is also shown with analogous slope values. All results are also shown for the LME with the ensemble mean subtracted (light-green and orange triangles for pluvial and droughts respectively). ** denotes significant slope values at the 5% level determined from phase-scrambling Monte-Carlo simulations

characterized by off-equatorial variability in addition to equatorial anomalies, thus the tripolar IPO index most accurately captures basin-wide internal variability (Capotondi et al. 2023; Henley et al. 2015; Power et al. 2021). We therefore choose to solely characterize Pacific decadal variability with the tripole IPO index for the remainder of this study in lieu of a decadal ENSO index. Indeed SST in the Nino3.4 region varies largely in-phase with the IPO on decadal timescales (r = 0.94, Supplementary Table 1).

Here we clarify the individual and combined influences of Pacific and Indian Ocean internal modes on MSEA rainfall extremes with specific consideration to non-linearities across phases. To assess the impact of each climate mode on the frequency of drought and pluvial extremes, we calculate the conditional probability of a rainfall extreme given each ocean basin's various climate states $P(R \mid O)$:

$$P(R \mid O) = \frac{P(R \cap O)}{P(O)} \tag{2}$$

where $P(R \cap O)$ is the joint probability of a rainfall extreme occurring concurrently with an ocean basin at a given state and $P(O)$ is the marginal probability of that ocean basin being at the same given state.

As an example, we estimate the conditional probability of MSEA drought extremes occurring when the IPO index is between 0.4 and 0.6. We first calculate the marginal probability of IPO $\in$ [0.4,0.6) defined as $P(O)$, which is estimated as the total number of years in the LME where IPO is between 0.4 and 0.6 (suppose there are 1,000 years) divided by the total number of pre-industrial years in the all-forcing LME (13,000 years) thus $P(O) = 1/13$. Then we estimate the joint probability of a drought extreme co-occurring with IPO $\in$ [0.4,0.6) defined as $P(R \cap O)$ as the number of years when MSEA rainfall is below the 2.5% threshold while IPO index is between 0.4 and 0.6 (suppose there are 100 years) divided by all LME years, thus $P(R \cap O) = 1/130$. Finally the conditional probability of drought extreme given the IPO state $P(R \mid O) = (1/130)/(1/13) = 10\%$.

We apply the above conditional probability framework to assess how the frequency of drought and pluvial extremes changes in response to Pacific and Indian Ocean decadal modes (IPO and IOD respectively). To do this, we assess how the conditional probability of MSEA drought extremes changes as the Pacific and Indian Ocean leading modes vary from their most negative to their most positive states (Fig. 5a, b). Similarly, we calculate the frequency of pluvial extremes across the spectrum of IPO/IOD index values in

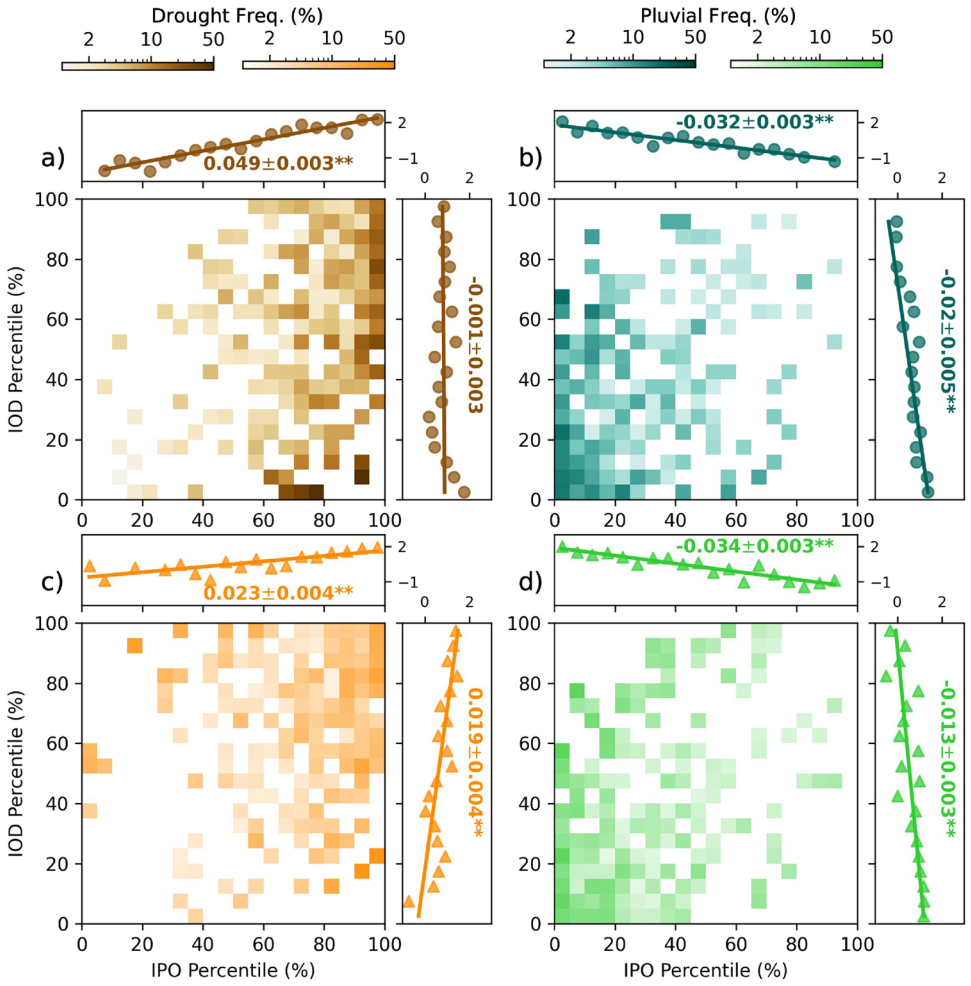

Fig. 6 Frequency of drought extremes as a function of both IPO (x-axis) and IOD (y-axis) percentile space in the center plot (colors) with the frequency along each axis shown in the marginal plots (circles) **(a)**. Corresponding plots for pluvial extremes **(b)** as well as for droughts **(c)** and pluvials **(d)** with the ensemble mean removed are also shown. Note that the color scale for center plots are in log-scale and the y-axis for marginal plots are in units of log[%], identical to Fig. 5. The slopes of marginal plot linear regressions are shown with one standard error (numbers). ** denotes significant slopes at the 5% level determined from Monte-Carlo phase scrambling

the LME (Fig. 5c, d). This conditional probability is systematically calculated across the percentile space of each climate index (IPO and IOD) in 650-year bins (5% quantiles, Fig. 5 circles/triangles). We choose to sample based on percentiles rather than absolute SST because percentile space is less sensitive to SST variance differences inherent between basins. These conditional probabilities increase exponentially as a function of IPO/IOD percentile, thus we log-transform them to linearize their change as a function of climate mode. From these linearized probabilities, we can quantitatively assess the sensitivity of MSEA rainfall extremes to various Indo-Pacific climate modes by examining the slopes of these distributions (Fig. 5a–d slopes). The conditional probabilities are calculated for both the original, all-forcing LME data which includes both external and internal forcings (Fig. 5 circles) as well as the LME with ensemble mean rainfall and SST values removed (Fig. 5 triangles). This allows us to elucidate how external forcings potentially modulate the relationships between SST modes and rainfall extremes.

In addition to assessing the frequency of extremes, we also evaluate how the severity or magnitude of rainfall anomalies varies depending on underlying IPO and IOD state (Fig. 5e for IPO and Fig. 5f for IOD). To do this, we calculate the average rainfall anomaly of each quantile-bin, identical to the quantiles sampled for conditional probability analysis, and determine its location in rainfall percentile space relative to the entire LME distribution. Dry anomalies (droughts) would fall below the 50th percentile while wet anomalies (pluvials) would be above. The changes in rainfall percentile space relative to IPO and IOD percentiles are largely linear, thus the sensitivities (slopes) of these relationships are calculated directly (Fig. 5c, d slopes). Like the conditional probability analysis, this is computed for both the original LME (circles) and the LME with ensemble mean removed (triangles). To evaluate potential asymmetries in the relationship between climate modes and rainfall severity, we calculate slopes for dry anomalies (0th-50th percentile) and wet anomalies (50th–100th percentile) separately (Fig. 5 e, f green vs brown slopes).

The significance of slope values are assessed by Monte-Carlo methods in which we phase scramble the rainfall data while keeping the climate index data the same, essentially decoupling rainfall from Indo-Pacific climate.

Frequency and severity analysis is then performed and slope values are calculated identical to the real data. This is repeated 1000 times to generate a null distribution of slope values for significance testing.

Focusing first on the IPO, we see that drought extremes frequency exhibits slightly higher (within one standard error) dependence on IPO state than pluvial extremes for the all-forcing LME (0.045 vs 0.039; Fig. 5a, b). With the removal of the ensemble mean, this discrepancy vanishes, suggesting that the frequency of MSEA drought and pluvial extremes is largely symmetric in their dependence on IPO state without external forcings. Interestingly, severity analysis reveals a stronger dependence of pluvials to IPO state than droughts (−0.72 vs −0.62 for original LME; Fig. 5e) although this modest discrepancy (within one standard error) decreases when the ensemble mean is removed (−0.69 vs −0.65; Fig. 5e).

When sampling the LME based on IOD state, we see that the sensitivity of drought extremes is much weaker than that of pluvial extremes for the LME with external forcings included (0.023 vs −0.033; Fig. 5b, d). When the ensemble mean is removed, this asymmetry flips and the slope for drought frequency is steeper than pluvials (0.035 vs −0.027; Fig. 5b, d). Similar to the IPO, sampling the IOD space for rainfall magnitude changes reveals a stronger sensitivity for pluvials than droughts (−0.52 vs −0.37; Fig. 5f) with a smaller difference once the ensemble mean is extracted (−0.54 vs −0.46; Fig. 5f).

These results highlight that IPO and IOD seem to exert nonlinear influences on MSEA drought and pluvial magnitude and frequency (Fig. 5) although IPO slope differences between wet and dry anomalies are largely within one standard error of each other. External forcings appear to also play a role in modulating rainfall dependencies on climate, especially in the Indian Ocean. It may be tempting to compare the slopes between the IPO and IOD relationships to assess the relative roles of each ocean basin, however doing so would assume independent behavior of IOD and IPO. Modeling and observational studies have previously shown that climate variability in the two basins are in-fact modestly coupled across a range of timescales due to tropical atmospheric teleconnections and the Indonesian Throughflow (Abram et al. 2020; Cai et al. 2019; Sprintall et al. 2020; Taschetto et al. 2020; Wang et al. 2024). Thus the analysis in Fig. 5 is limited in that it does not explicitly consider the interactions between ocean basins when estimating MSEA rainfall sensitivities. To mitigate this multicollinearity, we resample the LME to estimate the frequency of rainfall extremes (akin to Eq. 2) while considering the conditions of both ocean basins simultaneously. This multivariate conditional probability $P(R \mid O_I, O_P)$ is defined as:

$$P(R \mid O_I, O_P) = \frac{P(R \cap O_I \cap O_P)}{P(O_I \cap O_P)} \tag{3}$$

where O_I and O_P denote the IOD and IPO conditions, $P(R \cap O_I \cap O_P)$ is the joint probability of a rainfall extreme occurring at a given IOD and IPO state, and $P(O_I \cap O_P)$ is the joint probability of all years when IOD and IPO are at the corresponding state. Using Eq. 3 we systematically sample the LME and examine how the frequency of droughts and pluvials varies in IOD x IPO space. Figure 6 illustrates the distribution of drought and pluvial extremes in these two dimensions where each square corresponds to a 5% quantile (analogous to a scatterpoint in Fig. 5) for both the all-forcing LME (Fig. 6a, b) and the LME with the ensemble mean removed (Fig. 6c, d). These two-dimensional density maps (Fig. 6 center plots) can then be integrated along each axis to assess the sensitivity of rainfall extremes to one climate mode while explicitly controlling for the other (Fig. 6 marginal plots) resulting in slope values analogous to partial regression analysis (Fig. 6 numbers).

We see that the distribution of drought extremes in the original LME (Fig. 6a) increases rapidly as IPO becomes more positive (x-axis) but exhibits weak (insignificant) dependence to IOD (y-axis), confirmed by the slope of the marginal plots which are significant for former but not the latter (0.049 vs 0.001; Fig. 6a). Interestingly when external forcings are removed, the Indian Ocean plays a larger role in contributing to drought extremes (Fig. 6c) and the influence of the two basins are more comparable (0.023 and 0.019 for IPO and IOD; Fig. 6c). Both the IPO and IOD display significant relationships with pluvial frequency albeit the dependence on IPO is still stronger (−0.032 and −0.02; Fig. 6b). Unlike drought extremes, the slopes for pluvials remain largely consistent upon the removal of the ensemble mean (−0.034 and −0.013; Fig. 6d).

Similar to the frequency of extremes, we can assess how the severity of rainfall anomalies depends on both IPO and IOD through two dimensional sampling of both the all-forcing and internal-only LME (Fig. 7a, b). Here the color of each square corresponds to its position in rainfall percentile space and the marginal plots reflect their percentile change across each axis (IPO or IOD) independently. The slopes of the marginal plot relationships are split between wet and dry anomalies analogous to Fig. 5e, f to assess nonlinearities. In line with multivariate frequency analysis (Fig. 6), we observe that MSEA rainfall magnitude demonstrates insignificant dependence on IOD changes in the all-forcing LME (−0.08 and −0.11; Fig. 7a) which modestly improves when the external forcings are removed (−0.20 and −0.18; Fig. 7b). The Pacific Ocean, on the other hand, displays a strong relationship with MSEA rainfall across both droughts and pluvials with and without external forcings (Fig. 7a, b). Partial regression (added variable) analysis of un-binned

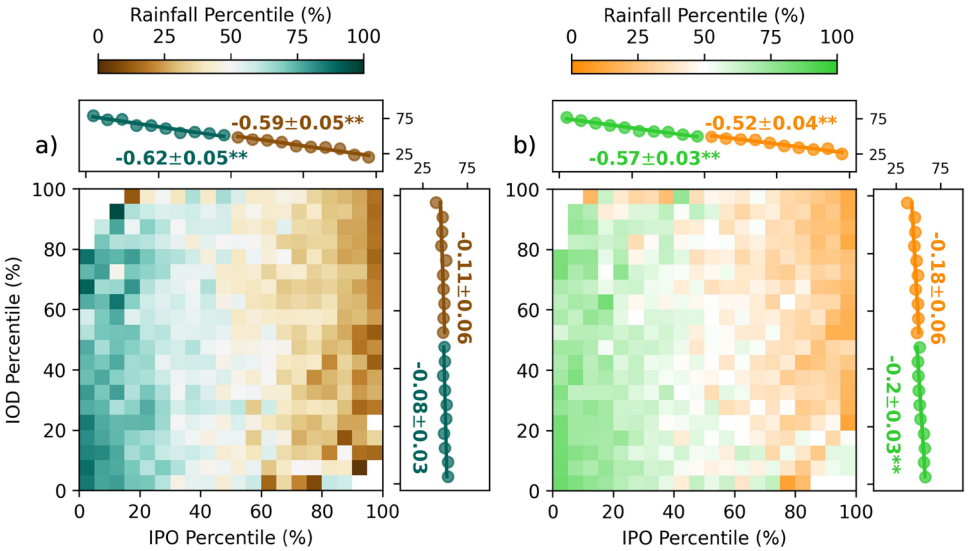

Fig. 7 Magnitude of rainfall anomaly in percentile space as a function of both IPO (x-axis) and IOD (y-axis) in the center plot (colors) and for each climate mode individually (marginal plots) in both the original LME **(a)** and upon subtraction of the ensemble mean **(b)**. The slope of the marginal plot relationships are shown with one standard error (numbers). ** denotes significant slopes at the 5% level determined from Monte–Carlo phase scrambling

IPO, IOD, and MSEA rainfall data reveals slope values that are consistent with our multivariate sampling analysis, indicating significant IPO partial slopes but largely not for IOD (Supplementary Table 2). Additionally, multivariate severity analysis is conducted on LME data with slightly shifted filter windows (10–40 years and 10–60 years) which resulted in largely identical results that highlight the robustness of these findings (Supplementary Fig. 8)

To contextualize the relationships between Indo-Pacific variability and MSEA hydroclimate, we examine the influence of climate modes on rainfall magnitude across all of monsoon Asia through the same bivariate sampling framework. Specifically we compute the rainfall percentile slopes for each climate mode (akin to Fig. 7 marginal plot slopes) for each gridpoint in monsoon Asia, providing a spatial perspective on the independent influence of each climate mode across the entire region (Fig. 8). Because the slope values in Fig. 7 across droughts and pluvials are within one standard error of each other (Fig. 7 brown vs green numbers), we assume linearity and compute a single slope value across dry and wet excursions (Fig. 8).

In agreement with Fig. 7severity analysis, we see significant negative relationships between IPO and rainfall in the MSEA region in the all-forcing LME (Fig. 8a) due to SST-driven changes in regional moisture transport and vertical ascent (Fig. 4). This IPO influence extends longitudinally through much of South Asia as well as into the western Pacific where its negative influence is strongest. Moving northward into central Asia, the IPO influence inverts (becomes positive) before switching back to a negative relationship around northern China and the Korean peninsula. This meridional tripole over Asia has been identified

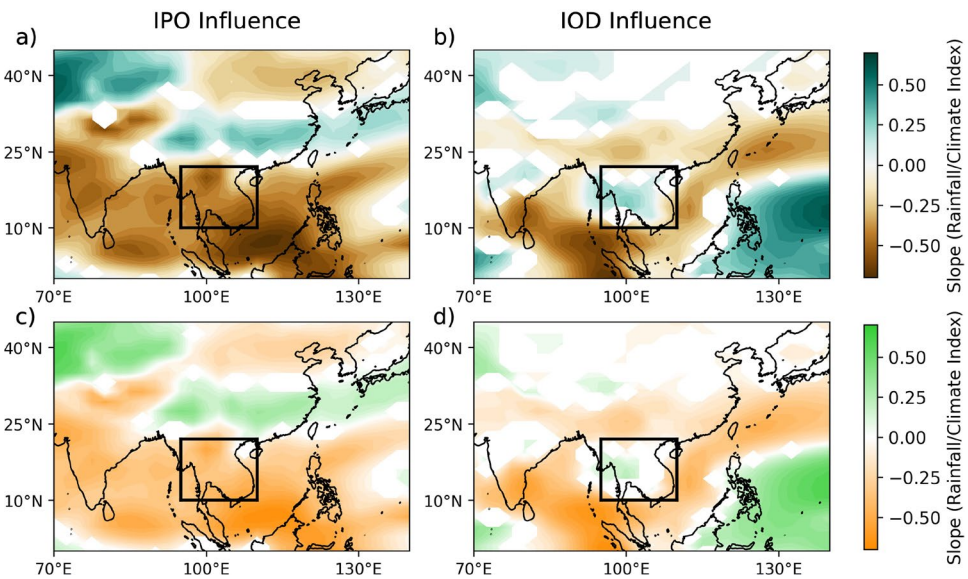

Fig. 8 Slopes from bivariate sampling and regression between IPO, IOD, and rainfall percentile anomalies across monsoon Asia (akin to Fig. 7). Marginal slopes are shown for the IPO **(a, c)** and IOD **(b, d)** using the all-forcing LME **(a, b)** as well as for whem the LME ensemble mean is removed LME **(c, d)**. The black box indicates the MSEA domain for rainfall analysis in this study. Only anomalies significant at the 5% level determined from Monte–Carlo phase scrambling are shown

in observational and paleoclimate studies (Gao et al. 2018, 2022; Li et al. 2017; Wang et al. 2013, 2024; Wen et al. 2019) as a result of equatorial Pacific warming which induces planetary waves that perturb the subtropical jet over Asia. The removal of external forcings does not change this spatial pattern meaningfully (Fig. 8c).

In contrast, the spatial footprint of IOD is more restricted to the tropics, with the most negative slope values in the eastern Indian Ocean where IOD-related upwelling off the coast of Sumatra is observed (Fig. 8b). The IOD's negative influence on rainfall extends westward into South Asia, consistent with previous studies of the Indian Summer Monsoon (Cherchi and Navarra 2013; Chongyin and Mingquan 2001). Critically, we observe a positive relationship between IOD and rainfall over MSEA and a negative relationship in Southern China (20° to 25°N). This is likely a result of IOD influences on the extension of the West Pacific Subtropical High which has previously been invoked to explain IOD-related impacts on Yangtze River Valley and South China rainfall (Chongyin and Mingquan 2001; Kripalani et al. 2010; Yuan et al. 2008). The ensemble mean removal does not dramatically change the IOD relationships with Asian monsoon rainfall except for a slight contraction of the positive relationship over MSEA (Fig. 8d), which may explain the modest increase in its influence between the datasets (Fig. 7a vs b).

This multivariate analysis illustrates that the IPO exerts a significant influence on MSEA rainfall extremes (while controlling for the Indian Ocean) whereas the IOD displays only weak to modest independent influence on MSEA extremes. Curiously we see that the subtraction of the ensemble mean appreciably enhances the IOD contributions to MSEA rainfall, especially for drought frequency (0.001 vs 0.019; Fig. 6a, c). Why might external forcings dampen the IOD relationship with MSEA rainfall? We suggest that this discrepancy can be attributed to volcanism-related impacts on Indo-Pacific climate and rainfall over Asia. Previous modeling work suggests that volcanic eruptions result in Northern Hemisphere surface cooling which intensifies the subtropical jet as well as the development of an El Niño event, both of which suppress the Southeast Asian monsoon and result in regional drying (Stevenson et al. 2016). Simultaneously, the volcanic cooling of tropical Africa excites atmospheric Kelvin waves that propagate eastward and enhance westerly winds over the Indian Ocean which favor the development of a -IOD event (Khodri et al. 2017; Izumo et al. 2018; Tiger and Ummenhofer 2023). Because -IOD is canonically associated with increased rainfall over monsoon Asia, the direct and El Niño-related volcanic impacts counteract the forced Indian Ocean hydroclimate response, weakening the observed relationship between IOD and MSEA rainfall. This also explains why drought frequency sensitivity to IOD increases markedly when external forcings are removed while the IOD influence on pluvials only slightly weakens (Fig. 6). Volcanism is not a symmetric forcing and there are no "negative volcanoes" that complement its drought impacts on Southeast Asia.

6 Last millennium external forcings

In this section we focus on how external forcings directly impact MSEA hydroclimate throughout the last millennium. The R_{IC} analysis (Eq. 1) highlighted several intervals where external forcings may have contributed to rainfall extremes (Fig. 3a). To comprehensively identify strong externally forced periods, we define a signal-to-noise ratio EF/IV:

$$EF/IV = \frac{R_{EM}}{\sigma_R} \tag{4}$$

where R_{EM} (like in equation 1) is the ensemble mean rainfall anomaly at a given timestep and σ_R is the standard deviation of rainfall anomalies across all 13 all-forcing ensemble members at the same timestep. This unitless ratio scales not only with the magnitude of ensemble mean anomaly but also with the amount of agreement between ensemble members. Most importantly EF/IV is agnostic to extreme event thresholds and strong externally forced periods emerge naturally. This EF/IV metric is consistent with our previous internal contribution (IC) definition as indicated by the strong negative correlations between the two (Supplementary Fig. 9). We compute EF/IV for the last millennium and contextualize its variability relative to historical MSEA droughts and tropical volcanic eruptions (Fig. 9). As in previous sections, the significance of EF/IV anomalies is assessed through Monte-Carlo phase-scrambling (Fig. 9 dashed lines). Over the last millennium, MSEA rainfall EF/IV generally remains quite low (between −0.5 to 0.5) but exhibits significant peaks (Fig. 9a) that often align with the timing of major volcanic eruptions (Fig. 9a triangles). This is consistent with previous studies of volcanic eruption impacts on tropical hydroclimate (Anchukaitis et al. 2010; Stevenson et al. 2016; Tejedor et al. 2021). To further assess the influence of volcanic forcings on MSEA hydroclimate, we also compute the EF/IV for the smaller volcanic forcing ensemble (n = 5) of the LME (Fig. 9b).

By comparing the EF/IV values to MSEA hydroclimate extremes identified from historical documentation and paleoclimate records (Buckley et al. 2014) (Fig. 9a, b gray shading), we gain insights into what forced these historical extremes. We see that the Angkor Drought 1 (1345–1374), Angkor Drought 2 (1401–1425), and the East Indian Drought (1790–1796) do not correspond to anomalously negative EF/IV periods in either the all-forcing or volcanic-forcing ensemble (Fig. 9a, b), suggesting that these droughts

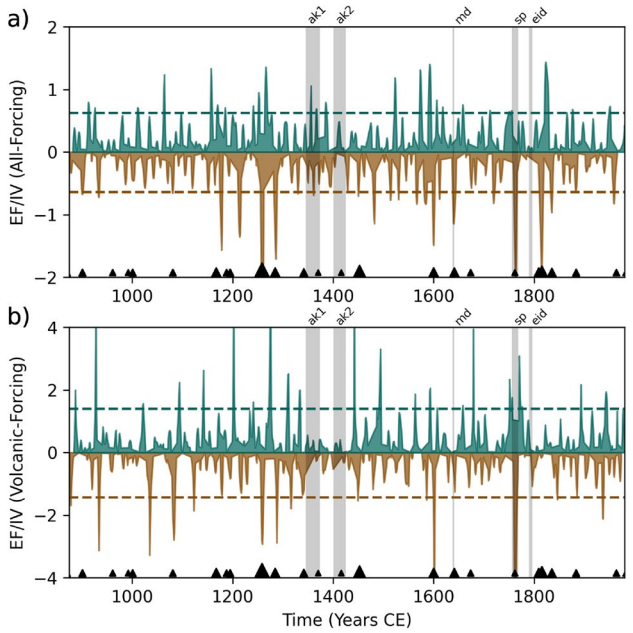

Fig. 9 The EF/IV metric, calculated using equation 4, as a function of time for the all-forcing ensemble (n = 13) **(a)** where positive (negative) EF/IV values are displayed in green (brown). EF/IV determined from the volcanic-forcing ensemble (n = 5) **(b)** is also shown. Dashed lines represent 95% significance thresholds determined from phase-scrambled Monte-Carlo simulations. Black triangles at the bottom of each plot represent tropical volcanic eruptions derived from (Gao et al. 2008) with the size of triangles scaling with estimated global sulfate aerosol injected (Tg). Following Tiger and Ummenhofer (2023), eruptions were identified as tropical if their Northern Hemisphere or Southern Hemisphere injections comprised less than 85% of the global total. The timing of historical droughts recorded in the MSEA region are indicated by gray shading. Historical drought acronyms: ak1,ak2-Angkor Droughts 1,2; md-Ming Dynasty Drought; sp-Strange Parallels Drought; eid-East India Drought

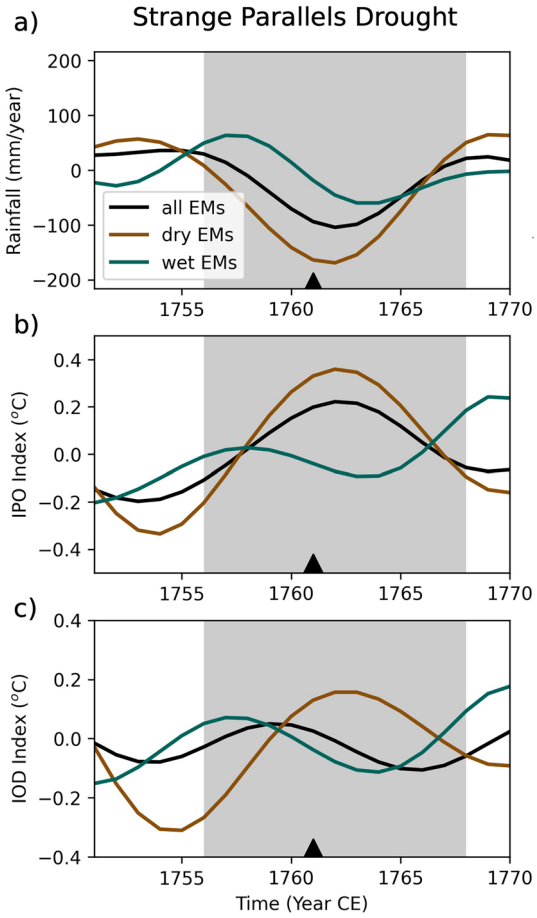

Fig. 10 The evolution of MSEA rainfall anomalies **(a)**, IPO index **(b)**, and IOD index **(c)** across the Strange Parallels Drought (1756–1768; grey shading) on decadal timescales (10–50 year band-pass filter). Results are shown for the all-forcing ensemble mean (black lines), average of three ensemble members with most intense decadal-scale Strange Parallels Drought response (brown lines) and average of three ensemble members with the weakest decadal-scale Strange Parallels Drought anomaly (green lines). A moderate tropical volcanic eruption is also indicated (black triangle)

may have been driven entirely by internal variability. On the other hand, the Ming Dynasty Drought (1638–1641) and Strange Parallels Drought (1756–1768) coincide with negative EF/IV excursions (significant in all-forcing) as well as moderately-sized tropical volcanic eruptions, suggesting that volcanic forcings contributed to these droughts. Consistent with our analysis, Chen et al. (2020) also found that a volcanic eruption contributed to the Ming Dynasty Drought using sensitivity climate simulations.

The Strange Parallels Drought severely affected various societies of 18th century South and East Asia (Buckley et al. 2007, 2014; Cook et al. 2010; Wang et al. 2019) due to its exceptional spatial and temporal scale. To our knowledge, we are the first to partially attribute this drought to a moderate volcanic eruption (estimated to have ejected roughly half the magnitude of sulfate aerosols as the 1991 Pinatubo eruption) which occurred during 1761 (Fig. 9), several years after the drought onset. The exact volcanic eruption responsible for the 1761 aerosol forcing in CESM-LME is unknown, as these forcings are derived retrospectively from ice core measurements (Gao et al. 2008; Otto-Bliesner et al. 2016). A more recently updated volcanic forcing dataset (eVolv2k; Toohey and Sigl 2017) shifted the timing of this mystery eruption to 1762, highlighting the uncertainty still present in precisely characterizing past eruptions. That volcanic forcings played a role in the Strange Parallels Drought is consistent with Yu et al. (2018) who found that the reconstructed drought pattern of the Strange Parallels Drought could not be purely ascribed to a combination of ENSO and IPO related hydroclimate anomalies. Similar to the findings of Chen et al. (2020) regarding the Ming Dynasty Drought, we argue that the Strange Parallels drought was driven by a combination of Indo-Pacific internal variability and a volcanic eruption. We explore how Indo-Pacific internal modes

modulate the externally forced signal of the Strange Parallels Drought by comparing between the three LME ensemble members with the weakest decadal-scale drought signals (wet EMs) to the three members with the strongest droughts (dry EMs; Fig. 10).

Across the three ensemble members with the strongest drought response (Fig. 10a brown line), both the Pacific and Indian Oceans were transitioning to a positive phase at the onset of the drought. These climate modes peaked simultaneously with MSEA rainfall anomalies (Fig. 10b, c), indicating that these in-phase internal modes enhanced the volcanically forced drought. For the simulations with the weakest droughts, the IPO and IOD indices were neutral or slightly negative throughout the Strange Parallels Drought, dampening the drought response. As shown here and in previous studies (Chen et al. 2020; Predybaylo et al. 2020; Tiger and Ummenhofer 2023), ocean prior state is important for modulating the hydroclimate response of external climate drivers, which may explain why only certain anomalous EF/IV periods coincide with observed historical droughts in the MSEA region (Fig. 10).

Not only can external forcings directly contribute to decadal-scale rainfall extremes, but they can also induce changes on timescales longer than their forcing through entrainment into lower frequency components of the climate system such as the global ocean overturning circulation. Indeed, changes in planetary radiative forcings are the leading proposed drivers of the Medieval Climate Anomaly (MCA, 950–1250 CE) and the Little Ice Age (LIA, 1500–1800 CE), two intervals of globally coherent changes in temperature and hydroclimate throughout the last millennium (Sinha et al. 2011; Mann et al. 2009). Here we assess whether the relationships between climate modes (IPO and IOD) and MSEA rainfall during these periods were exceptional relative to the natural variability of the last millennium. To do this, we subsample the all-forcing LME to target the two respective 300-year intervals (950–1250 CE and 1500–1800 CE) and compare their frequency and severity (identical to Sect. 5 analysis) to all other 300-year intervals within the LME (Fig. 11).

While the IPO influence on MSEA hydroclimate remains significant throughout the last millennium (Fig. 11a), there is variability in the amplitude of these relationships. We see that IPO-MSEA relationships are of greater amplitude (further away from the null-hypothesis) during the LIA relative to the MCA (blue stars vs red triangles; Fig. 11a) for all extremes metrics except for pluvial frequency. This discrepancy is consistent with enhanced and more frequent volcanism during the LIA relative to the preceding MCA (Mann et al. 2009) which would constructively enhance the teleconnection between tropical Pacific variability and MSEA rainfall (Stevenson et al. 2016; Sun et al. 2022). The Indian Ocean's relationship with MSEA rainfall also experiences variations

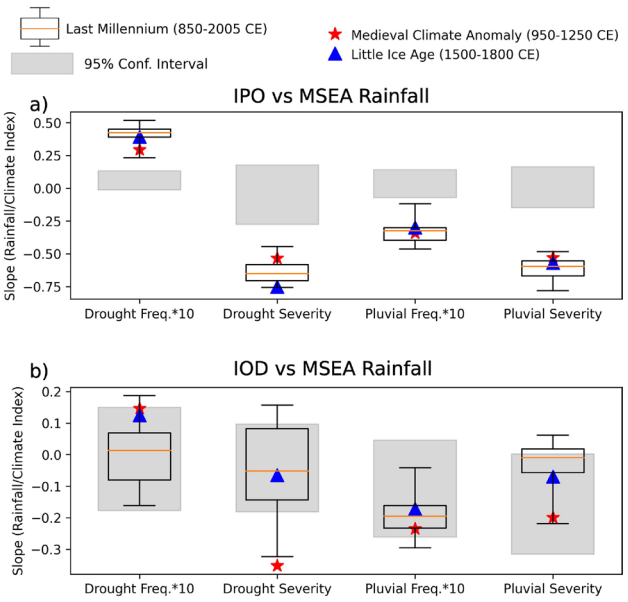

Fig. 11 The sensitivity (slope) of MSEA rainfall extremes to IPO **(a)** and IOD **(b)** state, calculated for each 300-year overlapping interval in the last millennium (boxplots), and with the Medieval Climate Anomaly (red star) and Little Ice Age (blue triangle) intervals highlighted. MSEA extremes frequency and severity are calculated in a bivariate framework for each 300-year bin using same methods as in Sect. 5. To better visualize all slopes on the same plot, frequency slope values were scaled by a factor of 10. Boxplot widths indicate the interquartile range of distribution with whiskers denoting 95% of the distribution. Gray shading denotes 95% confidence interval for significance testing, determined from phase-scrambling

though its marginal slope values remain largely insignificant throughout the last millennium (Fig. 11b). The sensitivity of MSEA extremes to IOD is stronger (higher magnitude) during the MCA than the LIA across all metrics, with MSEA drought severity slope actually significant at the 5% level (Fig. 11b). This complements the differences in relationship strength in the Pacific Ocean, suggesting that the enhanced volcanism of the LIA strengthened the IPO-MSEA teleconnection and weakened the IOD-MSEA relationship due to distinct volcanic impacts on MSEA hydroclimate and Indo-Pacific tropical modes. Notably, while the MCA-LIA discrepancies are consistent with previous studies, this analysis reveals that these two intervals do not represent the end-members of last millennium variability (Fig. 11 boxplots). Indeed for several metrics, such as IOD drought frequency and IPO pluvial severity, the differences between the MCA and LIA are quite modest relative to the entire distribution (Fig. 11). This may reflect more complex spatiotemporal Indo-Pacific variability beyond the simple dichotomy of the MCA and LIA. Recent data-model comparisons have suggested that last millennium climate simulations (including the CESM-LME) under-represent the amplitude of MCA-LIA

hydroclimate changes (Atwood et al. 2021) which calls for cautious interpretations of model-simulated centennial-scale variability.

7 Discussion and conclusions

The seasonal monsoon precipitation is critical for the 200 million people that reside in mainland Southeast Asia today, especially given that agriculture is one of region's most important economic sectors (Liu et al. 2020; Yuan et al. 2022). Decadal-scale variability in the monsoon rains can have long-term impacts on human health, infrastructure, and economy, as reflected by the historical multi-year droughts over the past millennium (Buckley et al. 2014; Penny et al. 2018). Thus the ability to assess and quantify drivers of low-frequency excursions in MSEA precipitation is essential. Here we utilized an ensemble of last millennium climate model simulations to explicitly quantify the contributions of Indo-Pacific internal modes (IPO and IOD) and external forcing to MSEA drought and pluvial extremes on decadal timescales (10–50 years).

Leveraging the ensemble of simulations, we find that internal variability dominated MSEA decadal extremes over the last millennium (Fig. 3) through modulation of the regional Indo-Pacific Walker circulation, resulting in atmospheric moisture transport and vertical velocity changes over the IPWP (Fig. 4). Utilizing a multivariate probabilistic framework, we find that both the frequency and severity of MSEA droughts and pluvials are significantly influenced by Pacific Ocean decadal variability (IPO; Figs. 5, 6). In contrast, SST gradients in the Indian Ocean (IOD) contribute minimally to MSEA rainfall extremes, which we partially attribute to volcanic eruptions that counteract forced IOD teleconnections. External forcings impacts, though small, are detectable and influence decadal-scale droughts more than pluvials (by roughly 10%; Figs. 3, 9). Specifically, we suggest that external forcing contributions during the last millennium are largely associated with major volcanic eruptions which suppress the Asian monsoon circulation (Fig. 9). We attribute volcanic forcing to two historical droughts: the Late Ming Dynasty Drought (1637–1643), consistent with a previous study (Chen et al. 2020), and the Strange Parallels Drought (1756–1768). This analysis does not identify significant externally forced influences to the 14th century Angkor Droughts, although definitive conclusions ruling out external drivers will require further investigation. In regards to the stationarity of these relationships between climate variability and rainfall, we find that Pacific (Indian) Ocean influences were weaker (stronger) during the MCA than the LIA, possibly mitigated by changes in volcanism across these two intervals that constructively (destructively) modulates these teleconnections (Fig. 11). We note that the MCA-LIA do not represent the bounds of last millennium variability, warranting more detailed investigation of spatiotemporal changes.

We present our findings, while highlighting caveats that are associated with the CESM-LME and global climate models broadly. First, CESM is known to exhibit biases in its spatiotemporal characterization of Indo-Pacific climate variability, producing a Pacific equatorial cold tongue that extends too far westward and eastern Indian Ocean SST that is too sensitive to upwelling (Jiang et al. 2021; Taschetto et al. 2014; Wieners et al. 2019; Wu et al. 2022) which likely influences inter-basin coupling and teleconnections to MSEA. Therefore while the relationships identified here likely translate qualitatively, we caution against interpreting their quantitative values as representative of the real climate system (see Sect. 3). Additionally, the magnitude of volcanic eruption impacts on tropical modes and hydroclimate is still under discussion. Modeling studies suggest an El Niño and -IOD like response to eruptions (Izumo et al. 2018; Khodri et al. 2017; Maher et al. 2015; Stevenson et al. 2016; Tiger and Ummenhofer 2023) which has been called into question by recent paleoclimate reconstruction studies (Dee et al. 2020; Zhu et al. 2022). These proxy studies instead suggest that climate models overestimate the magnitude of the forced volcanic response due to incomplete characterization of volcanic aerosol chemistry, inaccurate estimations of sulfate loading (LeGrande et al. 2016), and/or biased parameterization of ocean–atmosphere feedback processes. In light of these model deficiencies, the development of global climate simulations with increased spatial resolution, more complex atmospheric chemistry components, and accurate volcanic forcings is critical to mitigating these issues. In recent years, the emergence of paleoclimate data-assimilation which fuses real-world proxy information with the dynamically-consistent spatial covariance of climate models, provides another promising avenue to investigate past climate variability (Hakim et al. 2016; Steiger et al. 2018). By incorporating proxy information, these data-assimilation products have been shown to more realistically represent the timing and magnitude of hydroclimate responses to external forcings than climate models alone (Tejedor et al. 2021). Indeed, previous studies have utilized data-assimilation products such as the Last Millennium Reanalysis (LMR) and the Paleo-Hydrodynamics Data Assimilation (PHYDA) to study Asian monsoon variability over the past millennium (Du et al. 2023; Hu et al. 2023; Wang et al. 2024). In particular, Hu et al. (2023) identified correlations between Asian monsoon Palmer Drought Severity Index and Indo-Pacific SST in PHYDA and LMR that are largely consistent with the spatial composites of this study (Fig. 6 in Hu et al. 2023, Fig. 4g, h in this study), with IPO-like patterns in the Pacific and IOD-like patterns in the Indian Ocean. However, data assimilation itself is not without its biases as well, exhibiting sensitivity

to record density, proxy system models, and prior covariance stationarity (Amrhein et al. 2020; Sanchez et al. 2021). A more rigorous inter-dataset comparison should be conducted in the future, applying the various methodologies of this study to last millennium data-assimilation products (e.g., LMR, PHYDA) to corroborate the relationships derived solely from climate model simulations.

In spite of the structural biases associated with the CESM-LME, our probabilistic sampling is capable of recovering (and quantifying) previously identified relationships between the tropical Indo-Pacific, volcanism, and MSEA droughts/pluvials. The methods of this study provide an initial framework towards forecasting the frequency and severity of decadal-scale Southeast Asian rainfall extremes based on Pacific and Indian Ocean SST conditions. As discussed in the Introduction, Southeast Asia exhibits rainfall variability across a multitude of timescales. While this study provided key insights into the drivers of excursions on longer (decadal) timescales, functional water resource forecasting will require incorporation of shorter-timescale (intraseasonal to interannual) variability as well as the consideration of multi-scale interactions, for which these sampling methods can certainly be utilized for. The application towards ensemble simulations of future climate (e.g. CEMS-Large Ensemble and MPI Grand Ensemble; Kay et al. 2015; Maher et al. 2019) will be particularly important. However, there exist disagreements between climate models on the sign and amplitude of mean-state tropical hydroclimate modification under anthropogenic warming (Chen et al. 2020; Cook et al. 2022; Stevenson et al. 2022). We have shown that externally-forced changes over the past millennium (i.e. MCA vs LIA) can modulate the decadal-scale relationships between climate modes and MSEA rainfall (Fig. 11). Therefore reconciling the uncertainties in future mean-state hydroclimate changes will be critical for understanding long-term variability in the relationships between SST patterns and rainfall extremes.

Supplementary Information The online version contains supplementary material available at https://doi.org/10.1007/s00382-024-07412-x.

Acknowledgements Constructive comments by two anonymous reviewers and the editor are gratefully acknowledged. This study was supported by the U.S. National Science Foundation under AGS-2002083 (to CCU and SAM), AGS-2001949 (to BMB), OCE-2303513 (to CCU), and AGS-2302668 (to HTTN and BMB).

Funding Open Access funding provided by the MIT Libraries. This study was supported by the U.S. National Science Foundation under AGS-2002083 (to CCU and SAM), AGS- 2001949 (to BMB), OCE-2303513 (to CCU), and AGS-2302668 (to HTTN and BMB).

Availability of data and materials: All datasets used in this study are publicly accessible. Global Precipitation Climatology Centre (GPCC) were accessed at https://psl.noaa.gov/data/gridded/data.gpcc.html, Extended Reconstructed Sea Surface Temperature (ERSST) were accessed at https://www.ncei.noaa.gov/products/extended-reconstructed-sst, and the Hadley Centre Sea Ice and Sea Surface Temperature (HadISST) were accessed at https://www.metoffice.gov.uk/hadobs/hadisst/. The National Center for Atmospheric Research (NCAR) Paleoclimate Working Group is gratefully acknowledged for the CESM-LME, available at https://www.earthsystemgrid.org/dataset/ucar.cgd.ccsm4.cesmLME.html.

Declarations

Conflict of interest The authors have no conflicts of interests to declare.

References

Abram NJ, Wright NM, Ellis B, Dixon BC, Wurtzel JB, England MH, Ummenhofer CC, Philibosian B, Cahyarini SY, Yu TL, Shen CC, Cheng H, Edwards RL, Heslop D (2020) Coupling of Indo-Pacific climate variability over the last millennium. Nature 579(7799):385–392. https://doi.org/10.1038/s41586-020-2084-4

Amrhein DE, Hakim GJ, Parsons LA (2020) Quantifying structural uncertainty in paleoclimate data assimilation with an application to the last millennium. Geophys Res Lett 47(22):e2020. https://doi.org/10.1029/2020GL090485

Anchukaitis KJ, Buckley BM, Cook ER, Cook BI, D'Arrigo RD, Ammann CM (2010) Influence of volcanic eruptions on the climate of the Asian monsoon region. Geophys Res Lett 37:22. https://doi.org/10.1029/2010GL044843

Ashok K, Guan Z, Yamagata T (2001) Impact of the Indian Ocean dipole on the relationship between the Indian monsoon rainfall and ENSO. Geophys Res Lett 28(23):4499–4502. https://doi.org/10.1029/2001GL013294

Atwood AR, Battisti DS, Wu E, Frierson DMW, Sachs JP (2021) Data-model comparisons of tropical hydroclimate changes over the common era. Paleoceanogr Paleoclimatol 36:7. https://doi.org/10.1029/2020PA003934

Buckley BM, Anchukaitis KJ, Penny D, Fletcher R, Cook ER, Sano M, Nam LC, Wichienkeeo A, Minh TT, Hong TM (2010) Climate as a contributing factor in the demise of Angkor, Cambodia. Proc Natl Acad Sci 107(15):6748–6752. https://doi.org/10.1073/pnas.0910827107

Buckley BM, Fletcher R, Wang SYS, Zottoli B, Pottier C (2014) Monsoon extremes and society over the past millennium on mainland Southeast Asia. Quatern Sci Rev 95:1–19. https://doi.org/10.1016/j.quascirev.2014.04.022

Buckley BM, Palakit K, Duangsathaporn K, Sanguantham P, Prasomsin P (2007) Decadal scale droughts over northwestern Thailand over the past 448 years: links to the tropical Pacific and Indian Ocean sectors. Clim Dyn 29(1):63–71. https://doi.org/10.1007/s00382-007-0225-1

Buckley BM, Ummenhofer CC, D'Arrigo RD, Hansen KG, Truong LH, Le CN, Stahle DK (2019) Interdecadal Pacific Oscillation reconstructed from trans-Pacific tree rings: 1350–2004 CE. Clim Dyn 53(5–6):3181–3196. https://doi.org/10.1007/s00382-019-04694-4

Cai W, Wu L, Lengaigne M, Li T, McGregor S, Kug JS, Yu JY, Stuecker MF, Santoso A, Li X, Ham YG, Chikamoto Y, Ng B, McPhaden MJ, Du Y, Dommenget D, Jia F, Kajtar JB, Keenlyside N, Lin X, Luo JJ, Martín-Rey M, Ruprich-Robert Y, Wang G, Xie SP, Yang Y, Kang SM, Choi JY, Gan B, Kim GI, Kim CE, Kim S, Kim JH, Chang P (2019) Pantropical climate interactions. Science 363(6430):4236. https://doi.org/10.1126/science.aav4236

Capotondi A, McGregor S, McPhaden MJ, Cravatte S, Holbrook NJ, Imada Y, Sanchez SC, Sprintall J, Stuecker MF, Ummenhofer CC, Zeller M, Farneti R, Graffino G, Hu S, Karnauskas KB, Kosaka Y, Kucharski F, Mayer M, Qiu B, Santoso A, Taschetto AS, Wang F, Zhang X, Holmes RM, Luo JJ, Maher N, Martinez-Villalobos C, Meehl GA, Naha R, Schneider N, Stevenson S, Sullivan A, van Rensch P, Xu T (2023) Mechanisms of tropical Pacific decadal variability. Nat Rev Earth Environ 2:1–16. https://doi.org/10.1038/s43017-023-00486-x

Chan JCL, Zhou W (2005) PDO, ENSO and the early summer monsoon rainfall over south China. Geophys Res Lett 32:8. https://doi.org/10.1029/2004GL022015

Chen K, Ning L, Liu Z, Liu J, Yan M, Sun W, Yuan L, Lv G, Li L, Jin C, Shi Z (2020) One drought and one volcanic eruption influenced the history of China: the late ming Dynasty Mega-drought. Geophys Res Lett 47(16):e2020. https://doi.org/10.1029/2020GL088124

Chen Z, Zhou T, Zhang L, Chen Zhang W, Jiang J (2020) Global land monsoon precipitation changes in CMIP6 projections. Geophys Res Lett 47(14):e2019. https://doi.org/10.1029/2019GL086902

Cherchi A, Navarra A (2013) Influence of ENSO and of the Indian Ocean Dipole on the Indian summer monsoon variability. Clim Dyn 41(1):81–103. https://doi.org/10.1007/s00382-012-1602-y

Chongyin L, Mingquan M (2001) The influence of the Indian ocean dipole on atmospheric circulation and climate. Adv Atmos Sci 18(5):831–843. https://doi.org/10.1007/BF03403506

Cook BI, Buckley BM (2009) Objective determination of monsoon season onset, withdrawal, and length. J Geophys Res Atmos 114:23. https://doi.org/10.1029/2009JD012795

Cook BI, Smerdon JE, Cook ER, Williams AP, Anchukaitis KJ, Mankin JS, Allen K, Andreu-Hayles L, Ault TR, Belmecheri S, Coats S, Coulthard B, Fosu B, Grierson P, Griffin D, Herrera DA, Ionita M, Lehner F, Leland C, Marvel K, Morales MS, Mishra V, Ngoma J, Nguyen HTT, O'Donnell A, Palmer J, Rao MP, Rodriguez-Caton M, Seager R, Stahle DW, Stevenson S, Thapa UK, Varuolo-Clarke AM, Wise EK (2022) Megadroughts in the common era and the anthropocene. Nat Rev Earth Environ. https://doi.org/10.1038/s43017-022-00329-1

Cook ER, Anchukaitis KJ, Buckley BM, D'Arrigo RD, Jacoby GC, Wright WE (2010) Asian monsoon failure and megadrought during the last millennium. Science 328(5977):486–489. https://doi.org/10.1126/science.1185188

Dee SG, Cobb KM, Emile-Geay J, Ault TR, Edwards RL, Cheng H, Charles CD (2020) No consistent ENSO response to volcanic forcing over the last millennium. Science 367(6485):1477–1481. https://doi.org/10.1126/science.aax2000

Denniston RF, Ummenhofer CC, Wanamaker AD, Lachniet MS, Villarini G, Asmerom Y, Polyak VJ, Passaro KJ, Cugley J, Woods D, Humphreys WF (2016) Expansion and contraction of the indo-pacific tropical rain belt over the last three millennia. Sci Rep 6(1):34485. https://doi.org/10.1038/srep34485

Deser C, Phillips A, Bourdette V, Teng H (2012) Uncertainty in climate change projections: the role of internal variability. Clim Dyn 38(3):527–546. https://doi.org/10.1007/s00382-010-0977-x

Deser C, Phillips AS, Simpson IR, Rosenbloom N, Coleman D, Lehner F, Pendergrass AG, DiNezio P, Stevenson S (2020) Isolating the evolving contributions of anthropogenic aerosols and greenhouse gases: a new CESM1 large ensemble community resource. J Clim 33(18):7835–7858. https://doi.org/10.1175/JCLI-D-20-0123.1

Du X, Dee S, Hu J, Thirumalai K (2023) Solar irradiance modulates the Asian Summer Monsoon-ENSO relationship over the last millennium. Geophys Res Lett 50(23):e2023. https://doi.org/10.1029/2023GL105708

Ebisuzaki W (1997) A method to estimate the statistical significance of a correlation when the data are serially correlated. J Clim 10(9):2147–2153

Flato G, Marotzke J, Abiodun B, Braconnot P, Chou SC, Collins W, Cox P, Driouech F, Emori S, Eyring V, Forest C, Gleckler P, Guilyardi E, Jakob C, Kattsov V, Reason C, Rummukainen M et al. (2014) Evaluation of climate models. In: Climate Change 2013: The Physical Science Basis Contribution of Working Group I to the Fifth Assessment Report of the Intergovernmental Panel on Climate Change. Cambridge University Press, Cambridge, pp 741–866. https://doi.org/10.1017/CBO9781107415324.020

Fu H, Shi F, Liu W, Xue H, Man W, Li J, Guo Z (2024) Tracing the centennial variation of East Asian Summer Monsoon. Global Planet Change 238:104464. https://doi.org/10.1016/j.gloplacha.2024.104464

Gao C, Robock A, Ammann C (2008) Volcanic forcing of climate over the past 1500 years: An improved ice core-based index for climate models. J Geophys Res Atmos 113:23. https://doi.org/10.1029/2008JD010239

Gao Y, Chen D, Wang H, Ma J, Wang T (2022) Effect of interdecadal variation in southern Indian ocean SST on the relationship between ENSO and summer precipitation in the Asian-Pacific Monsoon Region. J Geophys Res Atmos 127:16. https://doi.org/10.1029/2021JD036151

Gao Y, Wang H, Chen D (2018) Precipitation anomalies in the Pan-Asian monsoon region during El Niño decaying summer 2016. Int J Climatol 38(9):3618–3632. https://doi.org/10.1002/joc.5522

Ge F, Zhu S, Sielmann F, Fraedrich K, Zhu X, Zhang L, Zhi X, Wang H (2021) Precipitation over Indochina during the monsoon transition: modulation by Indian Ocean and ENSO regimes. Clim Dyn 57(9–10):2491–2504. https://doi.org/10.1007/s00382-021-05817-6

Guilyardi E, Wittenberg A, Fedorov A, Collins M, Wang C, Capotondi A (2009) Understanding El Niño in Ocean-Atmosphere general circulation models: progress and challenges. Bull Am Meteorol Soc 90(3):325–340. https://doi.org/10.1175/2008BAMS2387.1

Hakim GJ, Emile-Geay J, Steig EJ, Noone D, Anderson DM, Tardif R, Steiger N, Perkins WA (2016) The last millennium climate reanalysis project: framework and first results. J Geophys Res Atmos 121(12):6745–6764. https://doi.org/10.1002/2016JD024751

Hariadi MH, van der Schrier G, Steeneveld GJ, Sutanto SJ, Sutanudjaja E, Ratri DN, Sopaheluwakan A, Klein Tank A (2024) A high-resolution perspective of extreme rainfall and river flow under extreme climate change in Southeast Asia. Hydrol Earth Syst Sci 28(9):1935–1956. https://doi.org/10.5194/hess-28-1935-2024

Hau NX, Sano M, Nakatsuka T, Chen SH, Chen IC (2023) The modulation of Pacific Decadal Oscillation on ENSO-East Asian summer monsoon relationship over the past half-millennium. Sci Total Environ 857:159437. https://doi.org/10.1016/j.scitotenv.2022.159437

Henley BJ, Gergis J, Karoly DJ, Power S, Kennedy J, Folland CK (2015) A tripole index for the interdecadal pacific

oscillation. Clim Dyn 45(11):3077–3090. https://doi.org/10.1007/s00382-015-2525-1

Hernandez M, Ummenhofer CC, Anchukaitis KJ (2015) Multi-scale drought and ocean-atmosphere variability in monsoon Asia. Environ Res Lett 10(7):074010. https://doi.org/10.1088/1748-9326/10/7/074010

Hrudya PPVH, Varikoden H, Vishnu RN (2021) Changes in the relationship between Indian Ocean dipole and Indian summer monsoon rainfall in early and recent multidecadal epochs during different phases of monsoon. Int J Climatol 41(S1):E305–E318. https://doi.org/10.1002/joc.6685

Hu J, Dee S, Parajuli G, Thirumalai K (2023) Tropical pacific modulation of the Asian summer monsoon over the last millennium in paleoclimate data assimilation reconstructions. J Geophys Res Atmos 128(20):e2023. https://doi.org/10.1029/2023JD039207

Hu P, Chen W, Wang L, Chen S, Liu Y, Chen L (2022) Revisiting the ENSO-monsoonal rainfall relationship: new insights based on an objective determination of the Asian summer monsoon duration. Environ Res Lett 17(10):104050. https://doi.org/10.1088/1748-9326/ac97ad

Huang B, Thorne PW, Banzon VF, Boyer T, Chepurin G, Lawrimore JH, Menne MJ, Smith TM, Vose RS, Zhang HM (2017) Extended reconstructed sea surface temperature, version 5 (ERSSTv5): upgrades, validations, and intercomparisons. J Clim 30(20):8179–8205. https://doi.org/10.1175/JCLI-D-16-0836.1

Izumo T, Khodri M, Lengaigne M, Suresh I (2018) A subsurface indian ocean dipole response to tropical volcanic eruptions. Geophys Res Lett 45(17):9150–9159. https://doi.org/10.1029/2018GL078515

Jiang W, Huang P, Huang G, Ying J (2021) Origins of the excessive westward extension of ENSO SST simulated in CMIP5 and CMIP6 models. J Clim 34(8):2839–2851. https://doi.org/10.1175/JCLI-D-20-0551.1

Jin C, Liu J, Wang B, Yan M, Ning L (2019) Decadal variations of the East Asian summer monsoon forced by the 11-year insolation cycle. J Clim 32(10):2735–2745. https://doi.org/10.1175/JCLI-D-18-0288.1

Kay JE, Deser C, Phillips A, Mai A, Hannay C, Strand G, Arblaster JM, Bates SC, Danabasoglu G, Edwards J, Holland M, Kushner P, Lamarque JF, Lawrence D, Lindsay K, Middleton A, Munoz E, Neale R, Oleson K, Polvani L, Vertenstein M (2015) The community earth system model (CESM) large ensemble project: a community resource for studying climate change in the presence of internal climate variability. Bull Am Meteor Soc 96(8):1333–1349. https://doi.org/10.1175/BAMS-D-13-00255.1

Khodri M, Izumo T, Vialard J, Janicot S, Cassou C, Lengaigne M, Mignot J, Gastineau G, Guilyardi E, Lebas N, Robock A, McPhaden MJ (2017) Tropical explosive volcanic eruptions can trigger El Niño by cooling tropical Africa. Nat Commun 8(1):778. https://doi.org/10.1038/s41467-017-00755-6

Kim IW, Oh J, Woo S, Kripalani RH (2019) Evaluation of precipitation extremes over the Asian domain: observation and modelling studies. Clim Dyn 52(3):1317–1342. https://doi.org/10.1007/s00382-018-4193-4

Kripalani RH, Oh JH, Chaudhari HS (2010) Delayed influence of the Indian Ocean Dipole mode on the East Asia-West Pacific monsoon: possible mechanism. Int J Climatol 30(2):197–209. https://doi.org/10.1002/joc.1890

Krishnamurthy L, Krishnamurthy V (2014) Influence of PDO on South Asian summer monsoon and monsoon-ENSO relation. Clim Dyn 42(9):2397–2410. https://doi.org/10.1007/s00382-013-1856-z

Krishnan R, Sugi M (2003) Pacific decadal oscillation and variability of the Indian summer monsoon rainfall. Clim Dyn 21(3–4):233–242. https://doi.org/10.1007/s00382-003-0330-8

LeGrande AN, Tsigaridis K, Bauer SE (2016) Role of atmospheric chemistry in the climate impacts of stratospheric volcanic injections. Nat Geosci 9(9):652–655. https://doi.org/10.1038/ngeo2771

Li G, Yu Z, Li Y, Yang C, Gu H, Zhang J, Huang Y (2024) Interaction mechanism of global multiple ocean-atmosphere coupled modes and their impacts on South and East Asian Monsoon: A review. Global Planet Change 237:104438. https://doi.org/10.1016/j.gloplacha.2024.104438

Li T, Wang B, Wu B, Zhou T, Chang CP, Zhang R (2017) Theories on formation of an anomalous anticyclone in western North Pacific during El Niño: a review. J Meteorol Res 31(6):987–1006. https://doi.org/10.1007/s13351-017-7147-6

Liu F, Gao C, Chai J, Robock A, Wang B, Li J, Zhang X, Huang G, Dong W (2022) Tropical volcanism enhanced the East Asian summer monsoon during the last millennium. Nat Commun 13(1):3429. https://doi.org/10.1038/s41467-022-31108-7

Liu J, Wang M, Yang L, Rahman S, Sriboonchitta S (2020) Agricultural productivity growth and its determinants in south and southeast Asian countries. Sustainability 12(12):4981. https://doi.org/10.3390/su12124981

Lu R, Dong B, Ding H (2006) Impact of the Atlantic multidecadal oscillation on the Asian summer monsoon. Geophys Res Lett 33:24. https://doi.org/10.1029/2006GL027655

Maher N, Lehner F, Marotzke J (2020) Quantifying the role of internal variability in the temperature we expect to observe in the coming decades. Environ Res Lett 15(5):054014. https://doi.org/10.1088/1748-9326/ab7d02

Maher N, McGregor S, England MH, Gupta AS (2015) Effects of volcanism on tropical variability. Geophys Res Lett 42(14):6024–6033. https://doi.org/10.1002/2015GL064751

Maher N, Milinski S, Suarez-Gutierrez L, Botzet M, Dobrynin M, Kornblueh L, Kröger J, Takano Y, Ghosh R, Hedemann C, Li C, Li H, Manzini E, Notz D, Putrasahan D, Boysen L, Claussen M, Ilyina T, Olonscheck D, Raddatz T, Stevens B, Marotzke J (2019) The Max Planck institute grand ensemble: enabling the exploration of climate system variability. J Adv Model Earth Syst 11(7):2050–2069. https://doi.org/10.1029/2019MS001639

Mann ME, Zhang Z, Rutherford S, Bradley RS, Hughes MK, Shindell D, Ammann C, Faluvegi G, Ni F (2009) Global signatures and dynamical origins of the little ice age and medieval climate anomaly. Science 326(5957):1256–1260. https://doi.org/10.1126/science.1177303

Milly PCD (1994) Climate, soil water storage, and the average annual water balance. Water Resour Res 30(7):2143–2156. https://doi.org/10.1029/94WR00586

Mohtadi M, Prange M, Steinke S (2016) Palaeoclimatic insights into forcing and response of monsoon rainfall. Nature 533(7602):191–199. https://doi.org/10.1038/nature17450

Narasimha R, Bhattacharyya S (2010) A wavelet cross-spectral analysis of solar-ENSO-rainfall connections in the Indian monsoons. Appl Comput Harmon Anal 28(3):285–295. https://doi.org/10.1016/j.acha.2010.02.005

Naveau P, Nogaj M, Ammann C, Yiou P, Cooley D, Jomelli V (2005) Statistical methods for the analysis of climate extremes. CR Geosci 337(10):1013–1022. https://doi.org/10.1016/j.crte.2005.04.015

Naveendrakumar G, Vithanage M, Kwon HH, Chandrasekara SSK, Iqbal MCM, Pathmarajah S, Fernando WCDK, Obeysekera J (2019) South Asian perspective on temperature and rainfall extremes: a review. Atmos Res 225:110–120. https://doi.org/10.1016/j.atmosres.2019.03.021

Nguyen HTT, Galelli S, Xu C, Buckley BM (2022) Droughts, pluvials, and wet season timing across the Chao Phraya River Basin: a 254-year monthly reconstruction from tree ring widths and d18O. Geophys Res Lett 49(17):e2022. https://doi.org/10.1029/2022GL100442

Otto-Bliesner BL, Brady EC, Fasullo J, Jahn A, Landrum L, Stevenson S, Rosenbloom N, Mai A, Strand G (2016) Climate variability and change since 850 CE: an ensemble approach with the community earth system model. Bull Am Meteor Soc 97(5):735–754. https://doi.org/10.1175/BAMS-D-14-00233.1

Penny D, Zachreson C, Fletcher R, Lau D, Lizier JT, Fischer N, Evans D, Pottier C, Prokopenko M (2018) The demise of Angkor: systemic vulnerability of urban infrastructure to climatic variations. Sci Adv 4(10):4029. https://doi.org/10.1126/sciadv.aau4029

Phan-Van T, Nguyen-Ngoc-Bich P, Ngo-Duc T, Vu-Minh T, Le PVV, Trinh-Tuan L, Nguyen-Thi T, Pham-Thanh H, Tran-Quang D (2022) Drought over Southeast Asia and its association with large-scale drivers. J Clim 35(15):4959–4978. https://doi.org/10.1175/JCLI-D-21-0770.1

Power S, Lengaigne M, Capotondi A, Khodri M, Vialard J, Jebri B, Guilyardi E, McGregor S, Kug JS, Newman M, McPhaden MJ, Meehl G, Smith D, Cole J, Emile-Geay J, Vimont D, Wittenberg AT, Collins M, Kim GI, Cai W, Okumura Y, Chung C, Cobb KM, Delage F, Planton YY, Levine A, Zhu F, Sprintall J, Di Lorenzo E, Zhang X, Luo JJ, Lin X, Balmaseda M, Wang G, Henley BJ (2021) Decadal climate variability in the tropical Pacific: characteristics, causes, predictability, and prospects. Science 374(6563):9165. https://doi.org/10.1126/science.aay9165

Predybaylo E, Stenchikov G, Wittenberg AT, Osipov S (2020) El Niño/Southern oscillation response to low-latitude volcanic eruptions depends on ocean pre-conditions and eruption timing. Commun Earth Environ 1(1):1–13. https://doi.org/10.1038/s43247-020-0013-y

Rayner NA, Parker DE, Horton EB, Folland CK, Alexander LV, Rowell DP, Kent EC, Kaplan A (2003) Global analyses of sea surface temperature, sea ice, and night marine air temperature since the late nineteenth century. J Geophys Res Atmos 108:14. https://doi.org/10.1029/2002JD002670

Roldán-Gmez PJ, González-Rouco JF, Melo-Aguilar C, Smerdon JE (2022) The role of internal variability in ITCZ changes over the last millennium. Geophys Res Lett 49:4. https://doi.org/10.1029/2021GL096487

Saji NH, Goswami BN, Vinayachandran PN, Yamagata T (1999) A dipole mode in the tropical Indian Ocean. Nature 401(6751):360–363. https://doi.org/10.1038/43854

Sanchez SC, Hakim GJ, Saenger CP (2021) Climate model teleconnection patterns govern the Niño-3.4 response to early nineteenth-century volcanism in coral-based data assimilation reconstructions. J Clim 34(5):1863–1880. https://doi.org/10.1175/JCLI-D-20-0549.1

Schneider U, Ziese M, Meyer-Christoffer A, Finger P, Rustemeier E, Becker A (2016) The new portfolio of global precipitation data products of the Global Precipitation Climatology Centre suitable to assess and quantify the global water cycle and resources. Proc IAHS 374:29–34. https://doi.org/10.5194/piahs-374-29-2016

Shi J, Yan Q, Wang H (2018) Timescale dependence of the relationship between the East Asian summer monsoon strength and precipitation over eastern China in the last millennium. Clim Past 14(4):577–591. https://doi.org/10.5194/cp-14-577-2018

Sinha A, Berkelhammer M, Stott L, Mudelsee M, Cheng H, Biswas J (2011) The leading mode of Indian Summer Monsoon precipitation variability during the last millennium. Geophys Res Lett 38:15. https://doi.org/10.1029/2011GL047713

Sinha A, Kathayat G, Cheng H, Breitenbach SFM, Berkelhammer M, Mudelsee M, Biswas J, Edwards RL (2015) Trends and oscillations in the Indian summer monsoon rainfall over the last two millennia. Nat Commun 6(1):6309. https://doi.org/10.1038/ncomms7309

Sinha A, Stott L, Berkelhammer M, Cheng H, Edwards RL, Buckley B, Aldenderfer M, Mudelsee M (2011) A global context for megadroughts in monsoon Asia during the past millennium. Quatern Sci Rev 30(1):47–62. https://doi.org/10.1016/j.quascirev.2010.10.005

Skliris N, Marsh R, Haigh ID, Wood M, Hirschi J, Darby S, Quynh NP, Hung NN (2022) Drivers of rainfall trends in and around Mainland Southeast Asia. Front Clim 4:5. https://doi.org/10.3389/fclim.2022.926568

Sprintall J, Cravatte S, Dewitte B, Du Y, Gupta AS (2020) ENSO oceanic teleconnections. In: McPhaden MJ, Santoso A, Cai W (eds) Geophysical monograph series, 1st edn. Wiley, New York, pp 337–359. https://doi.org/10.1002/9781119548164.ch15

Steiger NJ, Smerdon JE, Cook ER, Cook BI (2018) A reconstruction of global hydroclimate and dynamical variables over the Common Era. Sci Data 5(1):180086. https://doi.org/10.1038/sdata.2018.86

Stevenson S, Capotondi A, Fasullo J, Otto-Bliesner B (2019) Forced changes to twentieth century ENSO diversity in a last Millennium context. Clim Dyn 52(12):7359–7374. https://doi.org/10.1007/s00382-017-3573-5

Stevenson S, Coats S, Touma D, Cole J, Lehner F, Fasullo J, Otto-Bliesner B (2022) Twenty-first century hydroclimate: a continually changing baseline, with more frequent extremes. Proc Natl Acad Sci 119(12):e2108. https://doi.org/10.1073/pnas.2108124119

Stevenson S, Otto-Bliesner B, Fasullo J, Brady E (2016) "El Niño like'' hydroclimate responses to last millennium volcanic eruptions. J Clim 29(8):2907–2921. https://doi.org/10.1175/JCLI-D-15-0239.1

Sun W, Liu J, Wang B, Chen D, Gao C (2022) Pacific multidecadal (50–70 year) variability instigated by volcanic forcing during the Little Ice Age (1250–1850). Clim Dyn 59(1):231–244. https://doi.org/10.1007/s00382-021-06127-7

Supharatid S, Nafung J (2021) Projected drought conditions by CMIP6 multimodel ensemble over Southeast Asia. J Water Clim Change 12(7):3330–3354. https://doi.org/10.2166/wcc.2021.308

Taschetto AS, Gupta AS, Jourdain NC, Santoso A, Ummenhofer CC, England MH (2014) Cold tongue and warm pool ENSO events in CMIP5: mean state and future projections. J Clim 27(8):2861–2885. https://doi.org/10.1175/JCLI-D-13-00437.1

Taschetto AS, Ummenhofer CC, Stuecker MF, Dommenget D, Ashok K, Rodrigues RR, Yeh S (2020) ENSO atmospheric teleconnections. In: McPhaden MJ, Santoso A, Cai W (eds) Geophysical monograph series, 1st edn. Wiley, New York, pp 309–335. https://doi.org/10.1002/9781119548164.ch14

Tejedor E, Steiger NJ, Smerdon JE, Serrano-Notivoli R, Vuille M (2021) Global hydroclimatic response to tropical volcanic eruptions over the last millennium. Proc Natl Acad Sci 118(12):e2019. https://doi.org/10.1073/pnas.2019145118

Tiger BH, Ummenhofer CC (2023) Tropical volcanic eruptions and low frequency Indo-pacific variability drive extreme Indian ocean dipole events. Geophys Res Lett 50(19):e2023. https://doi.org/10.1029/2023GL103991

Toohey M, Sigl M (2017) Volcanic stratospheric sulfur injections and aerosol optical depth from 500 BCE to 1900 CE. Earth Syst Sci Data 9(2):809–831. https://doi.org/10.5194/essd-9-809-2017

Trenberth KE (1997) The definition of El Niño. Bull Am Meteorol Soc 78(12):2771–2777

Ummenhofer CC, D'Arrigo RD, Anchukaitis KJ, Buckley BM, Cook ER (2013) Links between Indo-Pacific climate variability and drought in the Monsoon Asia Drought Atlas. Clim Dyn 40(5):1319–1334. https://doi.org/10.1007/s00382-012-1458-1

Ummenhofer CC, Geen R, Denniston RF, Rao MP (2024) Past, present, and future of the South Asian monsoon. In: Ummenhofer CC, Hood RR (eds) The Indian Ocean and its Role in the Global Climate System. Elsevier, Amsterdam, pp 49–78. https://doi.org/10.1016/B978-0-12-822698-8.00013-5

Ummenhofer CC, Murty SA, Sprintall J, Lee T, Abram NJ (2021) Heat and freshwater changes in the Indian Ocean region. Nat Rev Earth Environ 2(8):525–541. https://doi.org/10.1038/s43017-021-00192-6

Vieira LEA, Solanki SK, Krivova NA, Usoskin I (2011) Evolution of the solar irradiance during the Holocene. Astron Astrophys 531:A6. https://doi.org/10.1051/0004-6361/201015843

Wang B, Wu R, Li T (2003) Atmosphere-warm ocean interaction and its impacts on Asian-Australian Monsoon variation*. J Clim 16(8):1195–1211

Wang B, Xiang B, Lee JY (2013) Subtropical high predictability establishes a promising way for monsoon and tropical storm predictions. Proc Natl Acad Sci 110(8):2718–2722. https://doi.org/10.1073/pnas.1214626110

Wang JK, Johnson KR, Borsato A, Amaya DJ, Griffiths ML, Henderson GM, Frisia S, Mason A (2019) Hydroclimatic variability in Southeast Asia over the past two millennia. Earth Planet Sci Lett 525:115737. https://doi.org/10.1016/j.epsl.2019.115737

Wang N, Dee S, Hu J, Steiger N, Thirumalai K (2024) PDO and AMO modulation of the ENSO-Asian summer monsoon teleconnection during the last millennium. J Geophys Res Atmos 129(1):e2023. https://doi.org/10.1029/2023JD039638

Wang Z, Li LZX, Shi X, Wang J, Jia J (2024) Influence of natural external forcings on interdecadal variation of global land monsoon over the last millennium in CESM-LME. J Clim 1:25. https://doi.org/10.1175/JCLI-D-23-0443.1

Webster PJ, Magaña VO, Palmer TN, Shukla J, Tomas RA, Yanai M, Yasunari T (1998) Monsoons: processes, predictability, and the prospects for prediction. J Geophys Res Oceans 103(C7):14451–14510. https://doi.org/10.1029/97JC02719

Wen N, Liu Z, Li L (2019) Direct ENSO impact on East Asian summer precipitation in the developing summer. Clim Dyn 52(11):6799–6815. https://doi.org/10.1007/s00382-018-4545-0

Wieners CE, Dijkstra HA, de Ruijter WPM (2019) The interaction between the Western Indian Ocean and ENSO in CESM. Clim Dyn 52(9):5153–5172. https://doi.org/10.1007/s00382-018-4438-2

Wu X, Okumura YM, DiNezio PN, Yeager SG, Deser C (2022) The equatorial pacific cold tongue bias in CESM1 and its influence on ENSO forecasts. J Clim 35(11):3261–3277. https://doi.org/10.1175/JCLI-D-21-0470.1

Xavier P, Rahmat R, Cheong WK, Wallace E (2014) Influence of Madden–Julian Oscillation on Southeast Asia rainfall extremes: observations and predictability. Geophys Res Lett 41(12):4406–4412. https://doi.org/10.1002/2014GL060241

Xiao HM, Lo MH, Yu JY (2022) The increased frequency of combined El Niño and positive IOD events since 1965s and its impacts on maritime continent hydroclimates. Sci Rep 12(1):7532. https://doi.org/10.1038/s41598-022-11663-1

Xu M, Xu H, Ma J, Deng J (2021) Impact of Atlantic multidecadal oscillation on interannual relationship between ENSO and East Asian early summer monsoon. Int J Climatol 41(4):2860–2877. https://doi.org/10.1002/joc.6994

Yang Y, Li J, Wu L, Kosaka Y, Du Y, Sun C, Xie F, Feng J (2017) Decadal Indian Ocean dipolar variability and its relationship with the tropical Pacific. Adv Atmos Sci 34(11):1282–1289. https://doi.org/10.1007/s00376-017-7009-2

Yu E, King MP, Sobolowski S, Otterå OH, Gao Y (2018) Asian droughts in the last millennium: a search for robust impacts of Pacific Ocean surface temperature variabilities. Clim Dyn 50(11):4671–4689. https://doi.org/10.1007/s00382-017-3897-1

Yuan S, Stuart AM, Laborte AG, Rattalino Edreira JI, Dobermann A, Kien LVN, Thúy LT, Paothong K, Traesang P, Tint KM, San SS, Villafuerte MQ, Quicho ED, Pame ARP, Then R, Flor RJ, Thon N, Agus F, Agustiani N, Deng N, Li T, Grassini P (2022) Southeast Asia must narrow down the yield gap to continue to be a major rice bowl. Nat Food 3(3):217–226. https://doi.org/10.1038/s43016-022-00477-z

Yuan Y, Yang H, Zhou W, Li C (2008) Influences of the Indian Ocean dipole on the Asian summer monsoon in the following year. Int J Climatol 28(14):1849–1859. https://doi.org/10.1002/joc.1678

Zheng J, Xiao L, Fang X, Hao Z, Ge Q, Li B (2014) How climate change impacted the collapse of the Ming dynasty. Clim Change 127(2):169–182. https://doi.org/10.1007/s10584-014-1244-7

Zhu F, Emile-Geay J, Anchukaitis KJ, Hakim GJ, Wittenberg AT, Morales MS, Toohey M, King J (2022) A re-appraisal of the ENSO response to volcanism with paleoclimate data assimilation. Nat Commun 13(1):747. https://doi.org/10.1038/s41467-022-28210-1